Dr. Karl Remeis-Sternwarte
Friedrich-Alexander-Universität
Erlangen-Nürnberg

Bachelorarbeit aus der Physik

Search for X-Ray Emission from SN1885A in M31

Vorgelegt von
Marie Prucker
04.07.2022

Betreuerin: Prof. Dr. Manami Sasaki

Abstract

In this work potential X-ray emission from the remnant of the historical supernova SAndromedae (SAnd or SN1885A) in M31 is investigated using Chandra HRC-I data, as so far no X-ray source has been reported at the position of SAnd. Prior to the data analysis, an overview of the history and previous observations of SAnd and its remnant is given. An upper limit on the X-ray luminosity of SNR1885 in the 0.1-10 keV band was obtained by analysing a total of 45 Chandra HRC-I observations. After applying astrometric corrections, the data was merged to create two separate images: one using all 45 observations and one using only 36 observations for which the calculated astrometric shifts did not exceed Chandra's pointing accuracy. For each image, the upper limit on the X-ray luminosity at the position of SAnd was calculated. The resulting values amount to $1.36 \times 10^{34}\,\mathrm{erg\,s^{-1}}$ (45 observations) and $1.53 \times 10^{34}\,\mathrm{erg\,s^{-1}}$ (36 observations). To contextualise these results, the upper limit obtained from combining all 45 observations was compared to the X-ray luminosities of four of the oldest known X-ray SNe, some younger Galactic remnants, some SNRs in M31 and to theoretical predictions. One finds that the upper limit on the X-ray luminosity of SNR1885 is two to three orders of magnitude lower compared to the examined other remnants. Comparison to theoretical predictions for the X-ray emission from SNe suggests that the evolution of SNR1885 is still largely dominated by the freely expanding ejecta. Either absorption or a low density surrounding medium could also account for the lack of X-ray emission. Furthermore, it was found that the X-ray luminosity might decrease faster towards the end of the ejecta-dominated phase in the evolution of SNRs than in the beginning. Lastly, the luminosity of a known Chandra source near SAnd was determined ($(4.2 \pm 0.9) \times 10^{34}\,\mathrm{erg\,s^{-1}}$ (36 observations); $(3.6 \pm 0.7) \times 10^{34}\,\mathrm{erg\,s^{-1}}$ (45 observations)). It is noted that as the Chandra source and SNR1885 are in such close proximity, the source's flux might have contributed to the obtained upper limit for SNR1885.

Contents

1. Introduction

Towards the end of August 1885 the discovery of the supernova (SN) SAndromedae (SAnd or SN1885A) in M31 caused a considerable stir amongst astronomers at the time. SAnd is still referred to as "the most fascinating event of modern astronomy" (Jones, 1976) and to this day, it is the first and brightest extragalactic SN ever observed (Jones, 1976).

Credit for the discovery of SAnd was given to the German astronomer Ernst Hartwig, who on 31 August 1885 made the first public announcement about the occurrence (Jones, 1976). Hartwig, who originally hailed from Frankfurt am Main, had accepted a position at the observatory in Dorpat, Estonia, one year prior in 1884, having been unhappy with the conditions at his previous position as assistant at the Strasbourg observatory. On 20 August 1885 he showed the Andromeda Nebula to some visitors with the great refractor at the Dorpat observatory, when he noticed the supernova for the first time, in his initial surprise calling it "a central sun in the nebula" (Greafe et al., 2015). However, due to the brightness of the moon that night, the Andromeda nebula was less visible than usual. Hartwig's superior at the time would not allow word to be sent to the astronomical news centre in Kiel without confirmation of the observation independent of the effects of a bright moon. This led to the public announcement being delayed by eleven days. In the meantime, numerous other reports about the observation of SAnd surfaced. However, it is save to say that Hartwig was the first to realise the significance of the event for modern astronomy (Jones, 1976). The discovery of SAnd can be considered a milestone in Hartwig's career. Shortly thereafter, he was offered the position of director at the at the time recently founded Remeis-Obseravtory in Bamberg, which he accepted in December 1885 as a now established independent observer (Greafe et al., 2015).

In the over 120 years since its discovery, SAnd has been studied extensively and a definitive visual light curve was presented based on available historical data (de Vaucouleurs and Corwin, 1985). The remnant of SAnd (SNR1885) was discovered in the optical in 1988 with the ground based telescope at Kitt Peak Observatory in Arizona (Fesen et al., 1989). Later, the Hubble Space telescope allowed even more detailed observations (Fesen et al., 1999, 2007). An upper limit on the radio luminosity of SNR1885 was determined based on observations with the Very Large Array (VLA) by Dickel and Dodorico (1984).

Thus far, no X-ray source has been observed at the position of SAnd. Detection of X-rays from the remnant would provide valuable information about the evolution of SNR1885 specifically but also about SNRs at this early stage and type I-SNe in general. Therefore, this work focuses on the search of X-ray emission from SNR1885 with data taken by NASA's Chandra X-ray observatory. In section 2, the necessary background information on SNe in general and on the evolution of supernova remnants (SNRs) is given, as well as a description of the Chandra X-ray observatory and its instruments. Next, section 3 provides a detailed overview of historical observations of SAnd, its classification and

more recent results of observations of the remnant in the optical, radio and X-rays. In section 4, the data analysis is presented in detail and the results are compared to the properties of some known Galactic and extragalactic SNRs. Finally, section 5 gives a summary of the obtained results.

2. Fundamental Information

2.1. Supernovae

During their life, main sequence stars produce energy by fusing hydrogen to helium in their cores, keeping them in hydrostatic equilibrium. Once the hydrogen is burned, helium-fusion sets in, producing carbon and oxygen. For stars with initial masses above 8 solar masses $M_\odot$, fusion continues, until an iron core is formed. In the case of lower mass stars around the mass of the sun, the collapse is halted by electron degeneracy pressure when the core consists of carbon and oxygen. The star is now white-hot at the surface and called a White Dwarf (WD). Unless the Chandrasekhar mass limit of $1.44\,M_\odot$ is reached, the star cannot evolve any further (Seward and Charles, 2010).

A star ends its life in a catastrophic explosion generally known as Supernova (SN). Depending on the optical properties of the explosion, one distinguishes two main types of SNe: type Ia/thermonuclear and type II. While type Ia-SNe are mainly characterised by the absence of hydrogen emission lines in their spectra, type II-SNe show broad hydrogen emission lines. Furthermore, there are notable differences between the respective light curves of the two SN-types as is shown in Figure 1. Within roughly two weeks, the luminosity L reaches its maximum of over $10^9\,L_\odot$. Following the maximum, the luminosity declines first rapidly and then more slowly until the SN eventually fades. The decay in brightness can be described exponentially with a characteristic time of around 55 days. Light curves of type Ia events are usually very similar, which hints at common types of progenitor stars and a common explosion mechanism. As the peak luminosity of type Ia-SNe is usually roughly the same as well, they can be used as standard candles to determine astronomical distances. The light curves of type II-SNe vary more, which indicates different progenitor stars and characteristics of the explosion. Compared to type Ia-SNe, the peak luminosity is about two orders of magnitude lower and the rise to maximum slower. The maximum itself is not quite as narrow as is the case for type Ia events (Seward and Charles, 2010).

Type Ia-SNe are believed to occur in binary systems consisting of a WD accreting mass from a companion star, until the WD reaches the Chandrasekhar limit ($\approx 1.44\,M_\odot$). At this point, the gravitational force exceeds the electron degeneracy pressure. As a result, the temperature rises until carbon and oxygen fusion is triggered, which causes an explosive wave, propagating through the core of the star within seconds. The nuclear fusion reactions initiated by the shock wave release about 10^{52} ergs of energy, which leads to the disruption of the star. Additionally, roughly $1\,M_\odot$ of radioactive ^{56}Ni is created in the process. The radioactive decay of the ejected ^{56}Ni explains the slower decline in

brightness after the initial rapid fall of brightness in the light curve of type Ia-SNe. Type II-SNe are most likely caused by the gravitational collapse of the core of the star and require an initial mass of at least $8\,M_{\odot}$ (Seward and Charles, 2010).

For the sake of completeness, it should be mentioned that type I-SNe in general also include the subtypes Ib and Ic. Similar to type II-SNe, types Ib and Ic are caused by the core collapse of a massive star but no hydrogen lines show in their spectra, which is what they have in common with type Ia-SNe (Jones, 1976). SN1885A, the source investigated in this work, is generally believed to be a type Ia event, as will be described in detail in subsection 3.2, which is why core collapse SNe will not be further discussed.

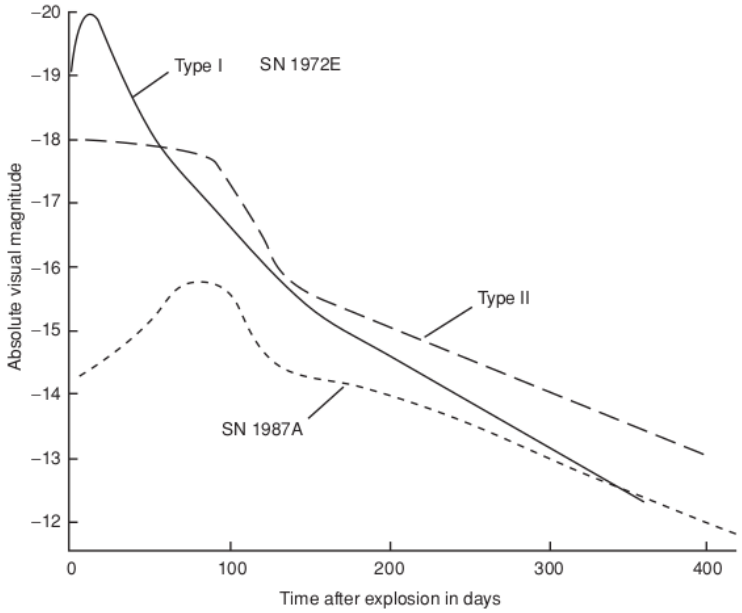

Figure 1: Light curves of three different SNe to illustrate the difference between type I (solid line: SN1972E, a type Ia event) and type II (dashed lines) light curves (Seward and Charles, 2010).

2.2. Evolution of Supernova Remnants

After some time, the SN itself fades and the transition to a Supernova Remnant (SNR) begins. The evolution of SNRs is generally divided into three different stages (see Figure 2), as will be discussed in further detail in the following.

2.2.1. Ejecta-Dominated Phase

The first phase in the evolution of a SNR is initiated by the SN-explosion and called the ejecta-dominated (ED) phase (Truelove and McKee, 1999). The shell of ejecta from

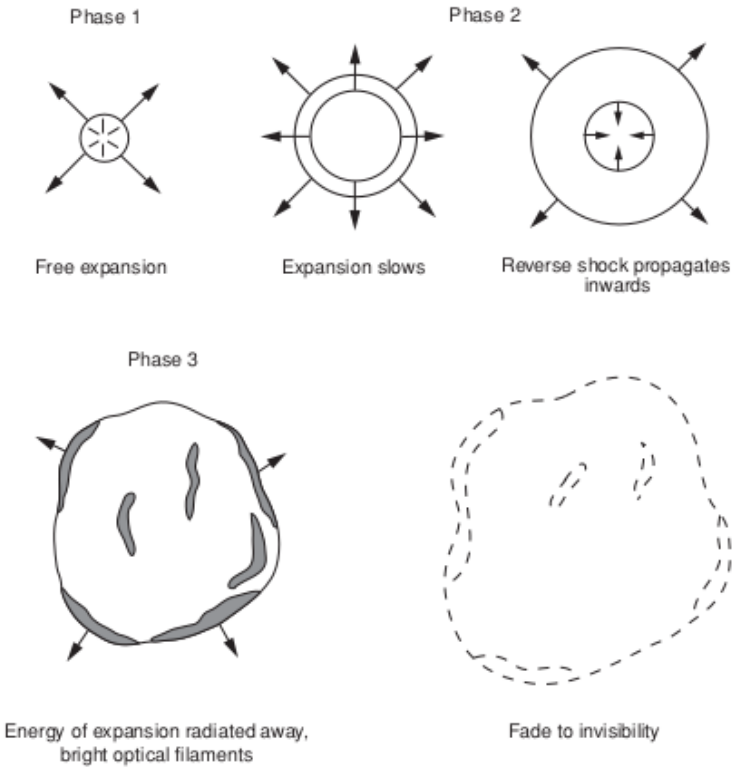

Figure 2: Schematic Illustration of the evolution of a SNR. Seward and Charles (2010)

the explosion sweeps up the surrounding interstellar medium (ISM), assuming equal expansion of the ejected material in all directions from the progenitor and a uniform surrounding medium (Seward and Charles, 2010). As the expansion velocity of the ejecta exceeds the sound speed in the surrounding gas, a shock wave (=blast-wave shock/forward shock) is created, preceding the ejecta and accelerating, compressing and heating the ambient gas. The ejecta in turn are decelerated, compressed and heated by the reverse shock, which is created by the shocked ambient gas pushing back into the ejecta at a significantly higher velocity than the speed of sound in the ejecta. Forward and reverse shock border at the so-called contact discontinuity. The unshocked ejecta in the centre of the remnant expand freely until they are hit by the reverse shock and accelerated inwards (Truelove and McKee, 1999). The mass of the ejecta M_{ej} exceeds the mass of the swept up medium M_{ISM} by far so that the evolution in this stage is largely dominated by the ejecta. Radiative losses in this phase are practically non-existent (Seward and Charles, 2010).

2.2.2. Sedov-Taylor Phase

The Sedov-Taylor (ST) phase is the second stage in the evolution of the SNR. The mass M_{ISM} of the medium swept up by the shock is now large in comparison to the ejecta-mass

M_{ej} and the shell expands adiabatically, with the expansion rate being determined by the explosion energy E_0 and the ISM-density ρ_{ISM} (Seward and Charles, 2010). Most of the energy from the ejecta has now been transferred to the ambient gas and the main difference to the previous phase is that the ejecta is no longer as important for the evolution of the remnant (Truelove and McKee, 1999). The forward shock propagates further outward into the ISM, and the reverse shock moves inwards. The material between the two shock waves is compressed and thereby heated enough to emit X-rays (Seward and Charles, 2010). Eventually, the reverse shock reaches the centre of the remnant and dissipates. Just like in the ED-phase radiative losses are considered insignificant for the dynamical evolution in this stage (Truelove and McKee, 1999).
It should be noted that in reality neither the ejecta nor the ISM are uniform, as was assumed in the beginning. The density in the ISM can vary or irregularities may have been caused by the stellar wind of the progenitor. Furthermore, even if the explosion runs symmetrically, the ejecta breaks into clumps due to the Rayleigh-Taylor instability (Seward and Charles, 2010).

2.2.3. Radiative Phase

In the third phase, most of the remnant's energy is released by radiation, thus it is called the radiative phase. The SNR expands further and an increasing amount of cool ISM is swept up by the shell. The temperature behind the shock decreases. Once it drops below 2×10^5 K, recombination of the electrons with the carbon and oxygen ions takes place, enabling UV-line emission. The radiative phase lasts for approximately 10^5 years, until eventually, the SNR fades completely into the ISM (Seward and Charles, 2010).

2.3. X-ray Emission from Supernovae

The thermal X-ray emission L_X from a SNR according to Ramakrishnan and Dwarkadas (2020) is given as follows:

$$L_X = \Lambda n_e^2 V \tag{1}$$

where Λ is the cooling function of the medium into which the shock is propagating, n_e is the electron density of the medium and V the volume of the emitting region. Chevalier (1982) presented a self-similar solution for the uniform expansion of gas into a stationary surrounding medium under the assumption that both media have power-law density profiles. This means the density of the ejecta ρ_{ej} and that of the circumstellar medium (CSM) ρ_{CMS} are described as (Ramakrishnan and Dwarkadas, 2020):

$$\begin{aligned} \rho_{ej} &\propto (\frac{r}{t})^{-n} t^{-3} \\ \rho_{CSM} &\propto r^{-s} \end{aligned} \tag{2}$$

Here, t stands for the passed time since the explosion and r is the distance to the explosion centre. The self similar solution only holds for power-law indices $n > 5$ and $s < 3$. As already mentioned, X-ray emission is assumed to originate only from a thin shell of shocked matter. The emission could come from either the forward or the reverse shock.

The radii of both shocks are proportional to the radius of the contact discontinuity r_c, which can be expressed as follows (Ramakrishnan and Dwarkadas, 2020):

$$r_c \propto t^{(n-3)/(n-s)} \tag{3}$$

If Equation 3 is inserted into Equation 2, one finds that the time dependence of the density of the shocked matter is the same for forward and reverse shock:

$$\rho_{ej/CSM} \propto t^{-s(n-3)/(n-s)} \tag{4}$$

The width Δr of the shell is proportional to its radius r_{sh}, which means the volume of the shocked matter V and the radius of the shock r_{sh} are connected via $V \propto r_{sh}^3$ (Ramakrishnan and Dwarkadas, 2020). The form of the cooling function Λ depends on the electron temperature T_e, which in turn depends on the shock velocity $v_{sh} \propto \frac{r_{sh}}{t}$ as $T_e \propto v_{sh}^2$. Using those relations, one obtains the following for the cooling function Λ (Chevalier and Fransson, 2017):

$$\begin{aligned} \Lambda &\propto T_e^{-0.48} \propto (r_{sh}/t)^{-0.96} && \text{for } T_e \leq 2.24\,\text{keV} \\ \Lambda &\propto T_e^{-0.5} \propto r_{sh}/t && \text{for } T_e > 2.24\,\text{keV} \end{aligned} \tag{5}$$

Combining Equation 3 and Equation 5 results in the following expressions for the X-ray luminosity L_X:

$$\begin{aligned} L_X &= L_0\, t^{-[(2s-3)n+6.12-5.04s]/(n-s)} && \text{for } T_e \leq 2.24 \\ L_X &= L_0\, t^{-[(2s-3)n+12-7s]/(n-s)} && \text{for } T_e > 2.24 \end{aligned} \tag{6}$$

In this case, L_0 is a proportionality factor with dimension $\text{erg}\,\text{s}^{-1}$. As is evident in Equation 2, n characterises the ejecta density and usually lies in the range $9 < n < 11$ for stellar envelopes (Matzner and McKee, 1999). The index s defines the density of the CSM, which is dependent on the stellar wind of the progenitor. Stellar winds are particle flows emitted from a star, which result in mass loss during its stable phase (ESA/Hubble, 2022). If the mass loss is constant over time, the wind is called a steady wind. In this case, the index $s = 2$ and Equation 6 can be written as follows (Ramakrishnan and Dwarkadas, 2020):

$$\begin{aligned} L_X &= L_0\, t^{-(n-3.96)/(n-2)} && \text{for } T_e \leq 2.24 \\ L_X &= L_0\, t^{-1} && \text{for } T_e > 2.24 \end{aligned} \tag{7}$$

In the Sedov-Taylor phase, the reverse shock reaches the centre of the SNR and only the forward shock remains and propagates further into the ISM. In the self similar solution, the radius r of the shock is given by (Ramakrishnan and Dwarkadas, 2020):

$$r \propto t^{-2/(5-s)} \tag{8}$$

This means for the CSM-density:

$$\rho_{CSM} \propto r^{-s} \propto t^{-2s/(5-s)} \tag{9}$$

The electron temperature T_e at this point can assumed to be below 2.24 keV. Therefore, the X-ray luminosity in the Sedov-Taylor phase can be expressed as follows:

$$L_X = L_0\, t^{(8.88-4.96s)/(5-s)} \tag{10}$$

L_0 is a again proportionality factor with dimension $\mathrm{erg\,s^{-1}}$. If it is assumed that the shock propagates into ISM with a density characterised by $s = 0$, Equation 10 becomes:

$$L_X = L_0\, t^{1.78} \tag{11}$$

This means L_X increases with time, because ρ_{ISM} is constant, while the volume of the shocked matter increases. The qualitative evolution of L_X over time is plotted in Figure 3 for $s = 2$ and $n = 10$ in the ED-phase and in Figure 4 for $s = 0$ in the Sedov-Taylor phase. Evidently, the luminosity decreases during the ED-phase and increases after transition to the Sedov-Taylor phase (Ramakrishnan and Dwarkadas, 2020).

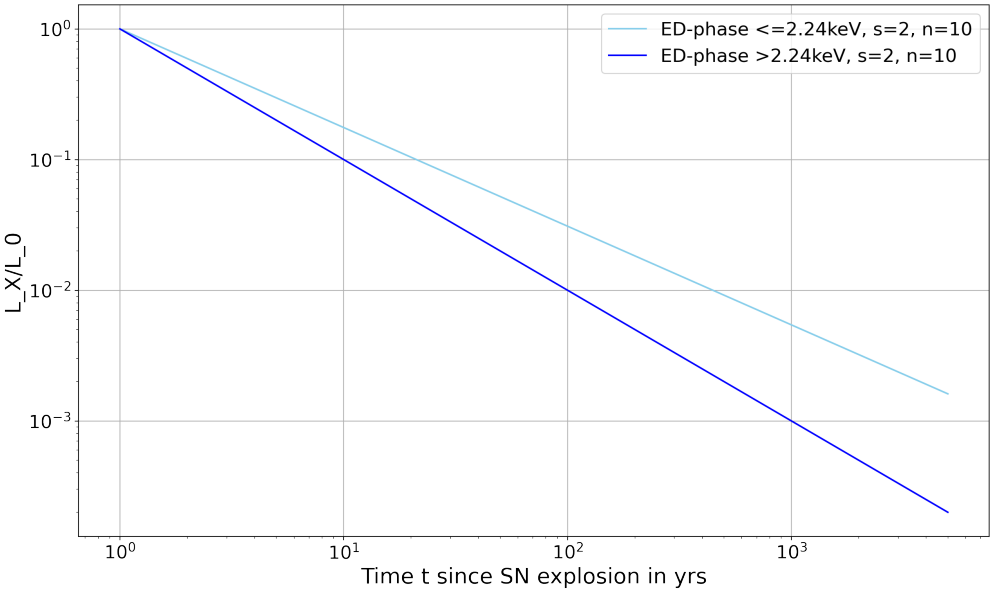

Figure 3: L_X/L_0 over the time t since the SN explosion according to Equation 7.

Figure 4: L_X/L_0 over the time t since the transition to the ST-phase according to Equation 11.

2.4. The Chandra X-Ray Observatory

The Chandra X-Ray Observatory (CXO) was launched by NASA on July 23, 1999 and is the space administration's flagship X-ray telescope. Chandra orbits above the atmosphere at an altitude of $\sim 6,000$ km at its closest up to $\sim 140,000$ km at its farthest distance from Earth. The exact orbit varies slightly with time (Chandra IPI Teams, 2022d). Approximately 75% of the satellite's elliptical orbit lies above the so-called Van Allen belts, which are rings of charged particles surrounding the Earth that would interfere with the observations otherwise (Harvard-Smithsonian Center for Astrophysics, 2014). Thereby, about 180 ks (~ 50 h) of uninterrupted observations are possible. A single orbit takes the spacecraft currently about 63.5 h (Chandra IPI Teams, 2022d).

Chandra is very well equipped for high resolution X-Ray imaging and spectroscopy, as illustrated schematically in Figure 5. X-rays are focused by the High Resolution Mirror Assembly (HRMA) located at the front of the spacecraft onto the respective detection instrument on the other side of the optical bench. The HRMA is made up of four pairs of iridium-coated, concentric glass mirrors installed on a support structure and has a focal length of 10 m, as schematically depicted in Figure 6. Each mirror is about 0.83 m long and the diameters range from 0.65 m to 1.23 m. In order for X-rays to be reflected at the mirror surface, the incidence angle needs to be extremely small. That is the case for so-called grazing-incidence mirrors, which are used in the HRMA. Each pair of mirrors consists of a parabolic mirror in the front and a hyperbolic mirror in the back, collectively forming a Wolter Type-I telescope (Chandra IPI Teams, 2022c).

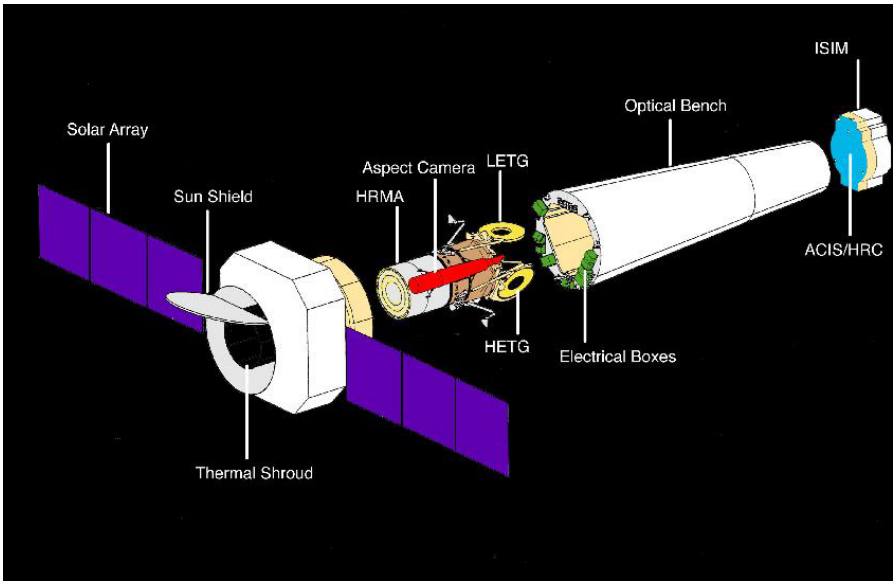

Figure 5: Schematic Illustration of Chandra Spacecraft Components. (Harvard Smithsonian Center for Astrophysics, 2008)

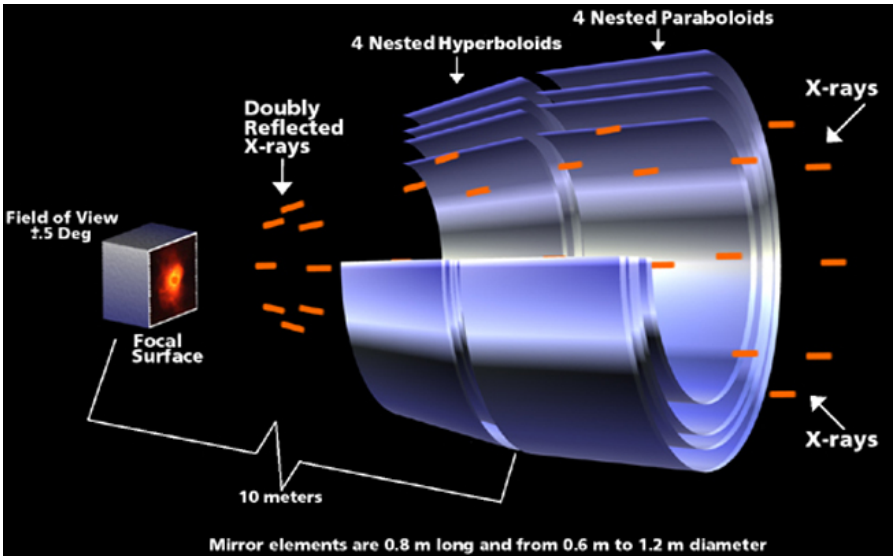

Figure 6: Schematic of the HRMA. The incident X-rays are focused onto the detection instrument by double reflection using a set of parabolic and a set of hyperbolic mirrors. (NASA/CXC/D.Berry, 2009)

The CXO possesses two different detection instruments: the Advanced CCD Imaging Spectrometer (ACIS) and the High Resolution Camera (HRC). ACIS can be used for

imaging with a resolution of ~ 0.5 arcsec, as well as spectroscopy and timing studies. The detector consists of two separate arrays of CCDs, ACIS-S and ACIS-I. ACIS-I is meant for imaging, while ACIS-S is better suited for moderate-resolution spectroscopy (Chandra IPI Teams, 2022a).

HRC is a microchannel plate (MCP) instrument and consists of two separate detectors, HRC-I and HRC-S as schematically depicted in Figure 7. HRC-S is meant for spectroscopy, while HRC-I is specifically designed for imaging (Chandra IPI Teams, 2022b). For the analysis later on in this work, Chandra HRC-I data are used. While HRC's intrinsic spectral resolution of $\Delta E/E \sim 1$ is lower than that of ACIS, the instrument operates over a slightly wider energy range (0.08-10 keV) and has a spatial resolution of 0.4 arcsec. Moreover, HRC-I's field of view covers an area of 30×30 arcmin, which is the largest among Chandra's detectors. In comparison, the field of view of HRC-S encompasses 6x99 arcmin. HRC also has the best timing resolution with 16 μs (Chandra IPI Teams, 2022b).

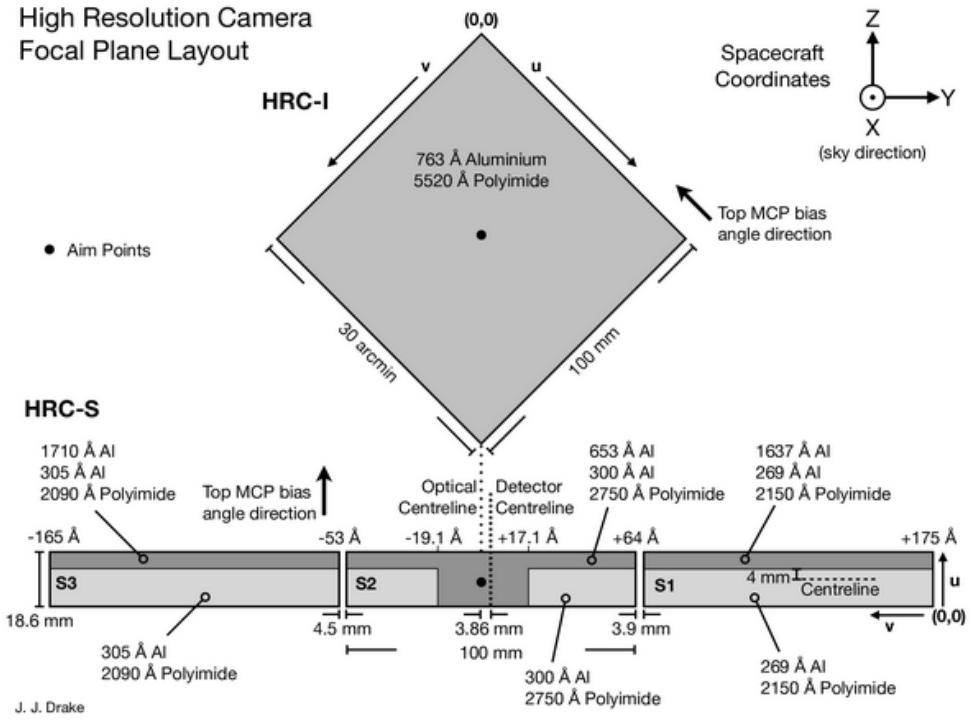

Figure 7: Schematic of the HRC focal-plane layout in the direction of the optical axis from the telescope towards the focal plane. (Chandra IPI Teams, 2022b)

Additionally, the telescope has two grating spectrometers available, namely the High Energy Transmission Grating (HETG) and the Low Energy Transmission Grating (LETG),

both of which can be alternately positioned behind the HRMA. The HETG is particularly designed for high-resolution spectroscopy over an energy range from 0.4 to 10 keV and is usually paired with ACIS-S, whereas the LETG operates at lower energies from 0.07 to 0.2 keV, ideally with HRC-S Chandra IPI Teams (2022d).

3. History of SAndromedae

3.1. Observations of SN1885A

The observation of SAndromedae (SAnd or SN1885A) was announced publicly for the first time on 31 August 1885 by Ernst Hartwig, who was astronomer at the Dorpat Observatory in Estonia at the time and later director of the Dr. Karl Remeis-Sternwarte in Bamberg Greafe et al. (2015). He messaged the astronomical news-centre in Kiel and claimed that "he had observed a distinct new star in the central region of M31" (Jones, 1976). Following the public announcement, numerous other reports about the appearance of a bright new star near the centre of the Andromeda Nebula prior to 31 August emerged. Several decades later, Hartwig revealed that he noticed the SN for the first time on 20 August 1885 in the 9 in Dorpat refractor and had refrained from addressing the public until he was able to confirm his observations. Hartwig measured visual magnitudes from at least 6 mag on 20 August to around 8 mag at the beginning of September. The first observation of SAnd was probably made by Professor Ludovic Gully at Rouen Observatory in France on the night of 17 August with the 20 cm Foucault telescope as the absence of a new star can be reliably confirmed before 10 pm on 16 August. M31 had been reported to appear unusually bright by several astronomers since the beginning of August 1885, one record even dating back to the beginning of July 1885. Gully was the first to notice an increase in brightness of M31 because of "a star in the place of the nucleus" (Jones, 1976) and estimated a visual magnitude of 5-6 mag. The object was commonly described to appear slightly yellow to orange in colour and compared to Arcturus or Aldebaran by a few sources. The SN remained visible for several months but eventually faded and was sighted for the last time on 7 February 1886. As Hartwig made the first public announcement about the occurrence and was the first to understand the importance of the observation, he was given credit for the discovery of SAnd (Jones, 1976).

A reconstruction of the light curve of SAnd using estimations of the visual magnitude from August to October 1885, including records from Hartwig and Gully, by Jones (1976) is displayed in Figure 8. In this case, all the available data in the respective time span were weighted equally, regardless of differences in measurement method or experience and ability of the observer. The maximum value for the visual magnitude m resulting from the graph lies at about 5.7 mag on 18/19 August, which is well in agreement with other reconstruction attempts, placing the maximum at 5.4 mag on 17/18 August (Gaposchkin, 1961). A visual magnitude of $m = 5.7$ mag corresponds to an absolute magnitude of $M = -18.5$ mag, assuming a distance modulus of $(m - M) = 24.2$ for M31 (Jones, 1976).

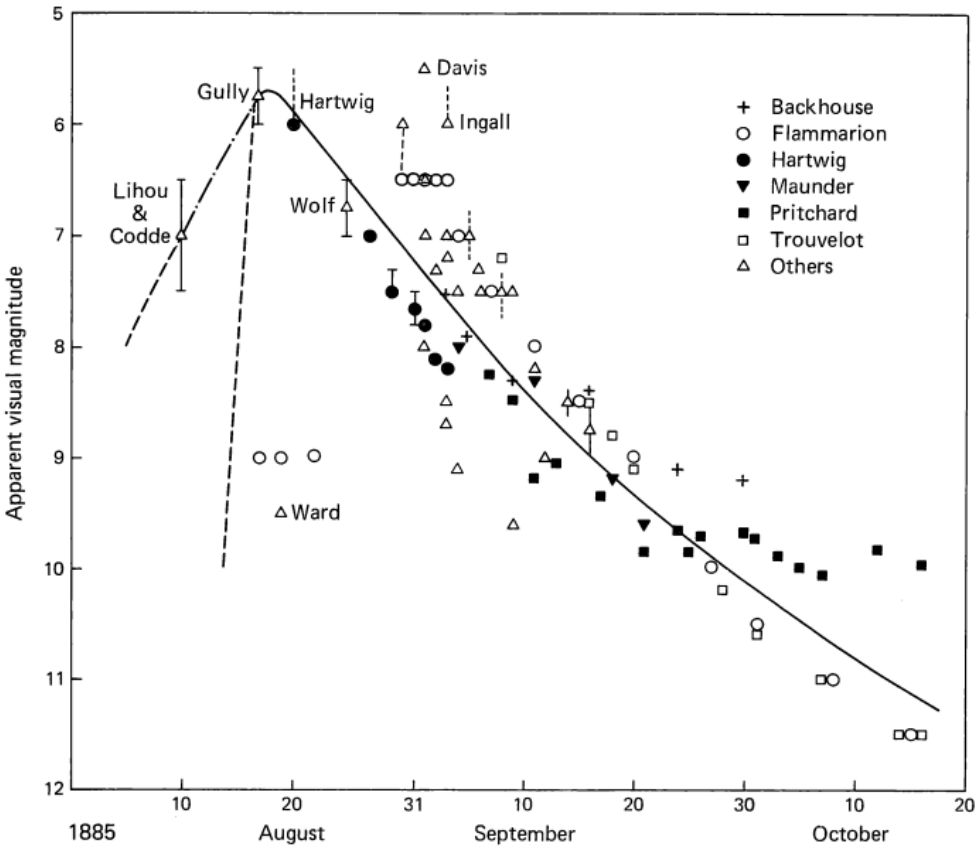

Figure 8: Reconstruction of the light curve of SN1885A from August to October 1885. The four measurements by Ward and Flammarion between 19 and 22 August as well as those by Davis and Ingall have been excluded from the analysis, as they differ significantly from the rest of the data. (Jones, 1976)

3.2. Classification of SN1885A

SAnd is generally believed to be a type Ia-SN based mainly on its spectral features. However, while sources widely agree on the classification as a type I-SN, determination of the sub-type is less agreed upon. The reason is SAnd's rather unusual light curve, as will be explained in the following.

A definitive visual light curve of SAnd (see Figure 9) was presented by de Vaucouleurs and Corwin (1985) after reviewing all the available data between the end of August 1885 and the beginning of March 1886. Furthermore, they performed a spectral analysis, which indeed revealed a good match of the detected emission lines with those expected in type Ia spectra. Hydrogen Balmer lines were also found to be absent, which is in agreement with previous spectroscopic observations for example by Gaposchkin (1936). The Fe I absorption in the remnant of SAnd observed by Fesen et al. (1989) provides

another argument for the classification as a type Ia-event.

However, de Vaucouleurs and Corwin (1985) also noted that SAnd was sub-luminous compared to other typical type I-SNe and has one of the fastest light curves ever recorded, especially with regard to the initial decline (2 mag in 12.5 days). Moreover, it is stated that the colour at maximum and in the two to three weeks thereafter is unusually red for a type I-SN ($B - V = +1.31 \pm 0.06$). Apart from the maximum, colour and luminosity evolve as expected. SAnd is classified as type I peculiar by de Vaucouleurs and Corwin (1985).

Graham (1988) compared the visual light curve of SN1885A to that of SN1984A, a type Ia event in NGC 4419. A striking similarity between the two SNe is found, based on which Graham classifies SAnd as type Ia despite its unusual light curve. The light curve of SN1984A, along with that of SN1885A presented by de Vaucouleurs and Corwin (1985), is shown in Figure 9. The classification as a type Ib is briefly considered and ruled out due to comparisons to spectra of other type Ib-events.

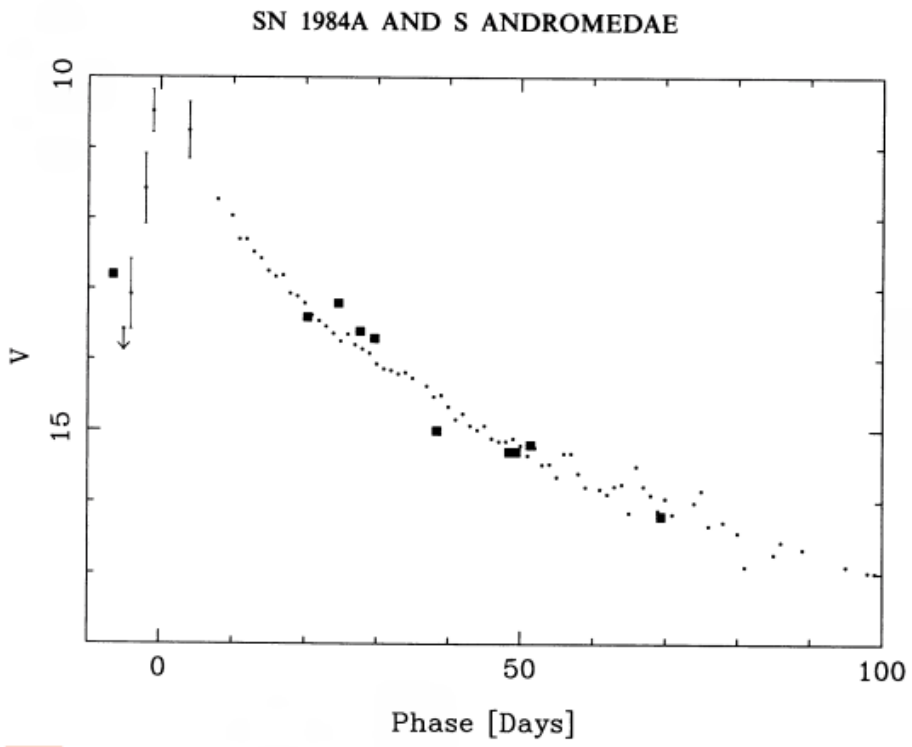

Figure 9: Visual light curves of SAnd (dots) and SN1984A (squares) (Graham, 1988). The light curve of SAnd is the one first presented by de Vaucouleurs and Corwin (1985).

Chevalier and Plait (1988) disagree with Graham (1988) and state in their work that SAnd is different from both type Ia and Ib for mainly three reasons, similar to those found by de Vaucouleur and Corwin: the rapid rise of the visual magnitude to maximum ($\sim$ 4 days from 3 mag below maximum to maximum; usual time scale for type I 14 ± 2 days), the rapid decline rate after maximum ($0.10 \pm 0.01\,\mathrm{mag\,day^{-1}}$; usually $0.065 \pm 0.007\,\mathrm{mag\,day^{-1}}$) and the large change in magnitude from maximum to 150 days post maximum ($\Delta m = 7.5$ mag; usually $\Delta m \approx 5$ mag). Due to model calculations, they assume a low mass explosion and combined with the assumption of an old stellar population in the bulge of M31, where the event took place, subsequently suggest a White Dwarf progenitor in a binary system.

Chevalier and Plait (1988) were not the only ones considering the possibility of SAnd belonging to some other sub-type of type I. The light curve of SN1885A was reexamined by van den Bergh (2002) and a classification as a sub-luminous type Ia event was considered based on the above mentioned unusual features of the light-curve and comparison to other sub-luminous type Ia-SNe. However, it is also suggested that SAnd could have been some other sub-type of type I-SNe.

3.3. The remnant of SN1885A

Despite the extensive search for the remnant of SAnd (SNR1885) in the optical and radio, it was not detected until a little over 100 years after the observation of the actual SN. The remnant was eventually discovered by Fesen et al. (1989) in optical absorption images within 1 arcsec of the historical location of SAnd in the bulge of M31. Following its discovery, the remnant was further investigated in the optical, radio and X-rays as is summarised hereinafter.

3.3.1. Optical Observations

As already mentioned above, SNR1885 was discovered in the optical by Fesen et al. (1989) with the ground based 4 m telescope at Kitt Peak National Observatory in Arizona. The images were taken on 9 November 1988, using two passband filters, creating "on" and "off" Fe I absorption images. The on-band filter was centred at $\lambda_c = 3908$ Å, covering the Fe I resonance line at $\lambda = 3860$ Å, while the off-band filter was shifted further to the blue ($\lambda_c = 3476$ Å) as to increase the visibility of regular dust lanes in M31. By creating a ratio image of on- and off-band images, absorption of dust is suppressed, thereby improving the visibility of the SNR itself. The resulting image is displayed in Figure 10. Fesen et al. (1989) concluded from their observations that SNR1885 was most likely still in the free expansion phase with largely cool, iron-rich ejecta. They estimated a maximal expansion velocity of $\pm 5000\,\mathrm{kms^{-1}}$ and placed SAnd on the side of the bugle of M31 facing us.

Later on, the SNR was studied in further detail with the Hubble Space Telescope (HST). On 7 August 1995, Fesen et al. (1999) again obtained Fe I ($\lambda = 3860$ Å) on- and off-band absorption images, using two different filters. Curiously, the remnant did not really

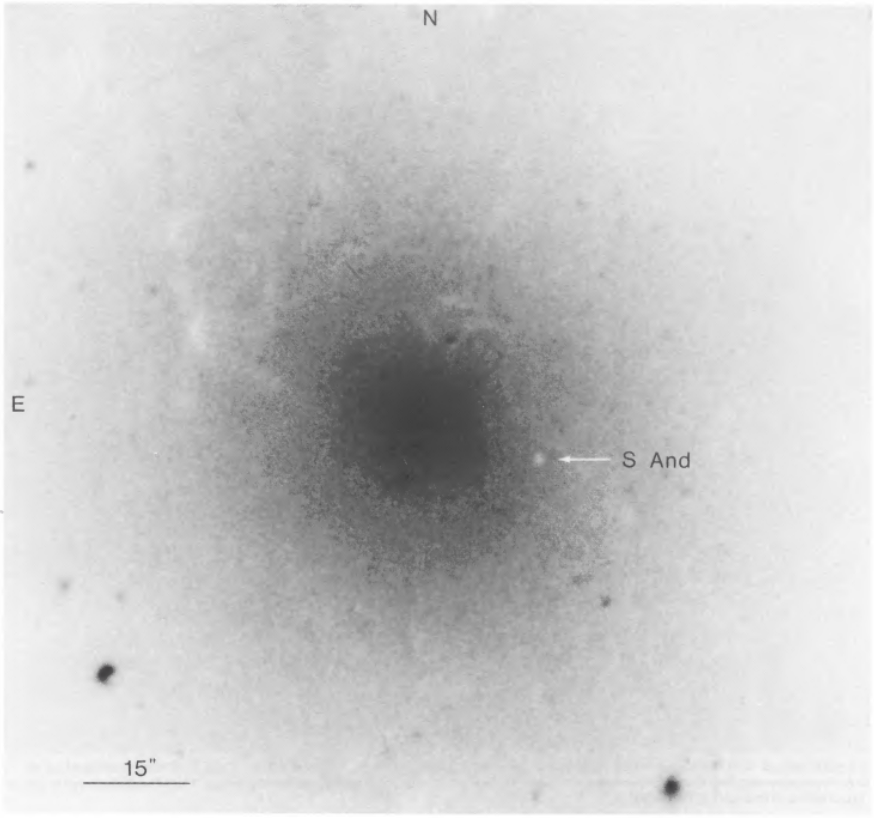

Figure 10: Ratio image of Fe I on- and off-band images. The arrow indicates the location of the remnant of SAnd. (Fesen et al., 1989)

show in the on-band images, but rather in the off-band images, where a dark absorption spot was visible at the location of SAnd. This led to the conclusion that the observed absorption was not largely due to Fe I, as previously assumed, but rather caused by Ca II at 3934 Å and 3968 Å for the most part. The absorption spectrum of SAnd was detected in December 1996. Aside from Ca II, absorption lines of Ca I (4227 Å) and Fe I (3934 Å) were identified. These low-ionised elements are well in agreement with the assumption of the ejecta being unshocked and freely expanding. A diameter of 0.70 ± 0.05 arcsec was measured, which implies an expansion velocity of $11,000 \pm 2,000\,\mathrm{kms}^{-1}$, if the distance to M31 is assumed to be 725 ± 70 pc. The expansion velocity was also estimated from the line profiles in the measured spectra and amounts to roughly $13,000 \pm 1,500\,\mathrm{kms}^{-1}$ (Fesen et al., 1999).

In 2007, Fesen et al. (2007) presented another optical study of SNR1885, analysing HST images with distinctly higher angular resolution than before. The observations took place between August and November in 2004 and allowed examination of the Ca and Fe distributions in the remnant as well as investigation of possible explosion scenarios. A variety of filters was used to obtain absorption images in different wavelength ranges.

These included absorption lines of Ca I, Ca II, a continuum band without strong absorption lines as well as Fe I and Fe II lines in UV. Four of the absorption images from Fesen et al. (2007) are displayed in Figure 11. After further processing, Fesen et al. found that Ca I absorption (Figure 11, top left) was strongest in the eastern and northern parts of the remnant in the direction of the nucleus of M31. The diameter in Ca I absorption was determined to be about 0.65 arcsec, which corresponds to 2.5 pc assuming a distance of 785 kpc to M31. The remnant turned out to be visible best in Ca II H and K line absorption (Figure 11, top right). Further analysis revealed Ca II absorption "clumps" of about 0.5 arcsec in size (~ 0.20 pc at 785 kpc). In the paper, the existence of a "broken ring of Ca II clumps" at a radius of about 0.2 arcsec is proposed. Apart from the clump structures the Ca II absorption seemed to be fairly even within a radius of 0.2 arcsec. The remnant appears to be spherical in Ca II absorption and the diameter of the entire absorption feature was measured to be about 0.80 ± 0.05 arcsec, so larger compared to Ca I absorption. The angular size corresponds to a diameter of 1.52 ± 0.15 pc at a distance of 785 ± 30 kpc to M31, implying an expansion velocity of $12,400 \pm 1400\,\mathrm{km\,s^{-1}}$. This value matches the expansion velocity obtained from the spectra in Fesen et al. (1999) ($13,000 \pm 1500\,\mathrm{kms^{-1}}$), which further indicates that SNR1885 is freely expanding. As for Fe I absorption, the image on the bottom left hand side in Figure 11 shows an uneven absorption spot about 0.6 arcsec in size with the absorption being strongest towards the northeast of the remnant, which is fairly similar to the observed Ca I absorption. The distribution of Fe II absorption (Figure 11, bottom right) largely resembles that of Ca II in size and shape (Fesen et al., 2007).

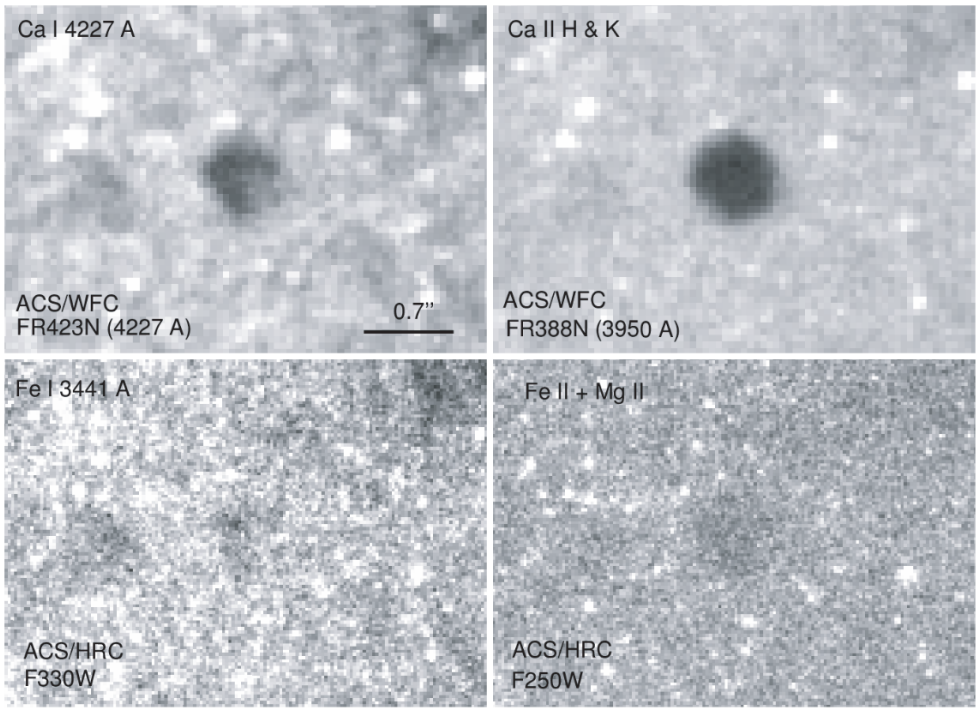

Figure 11: HST images of SNR1885 in Ca I ($\lambda = 4227\,$Å, top left), Ca II H and K ($\lambda = 3934\,$Å, $\lambda = 3968\,$Å; top right), FeI ($\lambda = 3441\,$Å, $\lambda = 3720\,$Å; bottom left) and Fe II + Mg II ($\lambda = 2358\,$Å, $\lambda = 2599\,$Å; $\lambda = 2800\,$Å; bottom right) . (Fesen et al., 2007)

3.3.2. Radio and X-Ray Emission

As of today, the remnant of SAnd has neither been detected in radio nor in X-rays. Radio observations of M31 with the Very Large Array (VLA) have, however, allowed to obtain an upper limit on the luminosity at the reported location of SAnd. Dickel and Dodorico (1984) presented a radio study of SNRs in M31 at a wavelength of 6.1 cm in 1983 and determined an upper limit of 0.2 mJy within a beam of $1.3 \cdot 1.0\,\mathrm{arcsec}^2$. This corresponds to a luminosity of less than $1 \times 10^{23}\,\mathrm{erg\,s^{-1}\,Hz^{-1}}$ at 6 cm, assuming a distance of 800 kpc to M31. In the paper, it is noted that this value is about two orders of magnitude smaller than the values determined for other historical type I-SNe in NGC 5253, about 0.4 times the luminosity of Tycho and 1.3 times that of Kepler.

Observations of M31 with the Chandra X-Ray Observatory by Kaaret (2002) reveal an X-ray source in close proximity to the location of SAnd. However, alignment of the X-ray images with HST observations places the source 1.3 arcsec ($\hat{=}\,4.9\,$pc at distance of M31) from the position of the in subsubsection 3.3.1 mentioned optical absorption feature identified as SNR 1885. This indicates that the source is not the X-ray counterpart of the remnant. In near UV HST images, a bright point source is visible within 0.15 arcsec

of the discovered X-ray source, which gives further reason not to associate the Chandra source with SAnd. Based on its estimated flux ($3.5 \cdot 10^{-16}\,\mathrm{erg\,s^{-1}\,cm^{-2}\,\AA^{-1}}$), the source is suspected to be an optical nova instead. This X-ray source will be discussed in detail in subsection 4.4.

4. Data Analysis and Results

For the data analysis presented in this chapter, Chandra HRC-I data from 48 different observations of M31 between 2001 and 2012 were downloaded from the Chandra data archive [1] and processed using CIAO versions 4.12 and 4.14. CIAO is a software package provided by the Chandra X-Ray Centre and was developed specifically for the analysis of Chandra data. It is freely available for download on the CIAO website[2]. Initially, three of the data sets had to be discarded, as there seemed to be a problem with the raw data that prevented further processing, leaving 45 observations for the actual analysis (see subsection B.1). As this is a fairly large amount of data sets, the individual CIAO tools were run from within Python, using the ciao contrib.runtool module. As part of the CIAO scripts package, the module allows to incorporate CIAO commands into Python scripts (see subsection B.2), which proved to be useful to loop over multiple data sets. A detailed documentation and the analysis guides consulted over the course of this work can be found on the CIAO website[3].

In a first step, each data set was reprocessed using the 'chandra_repro' script in order to recalibrate the data and create new level=2 event files, as is recommended in the analysis guides. To investigate potential X-ray emission from the remnant of SAnd, a merged image of the central region of M31 needed to be created. The necessary analysis steps and data preparation are described in the following.

4.1. Astrometric Corrections

Prior to merging the observations, astrometric corrections need to be applied to each data set to ensure all the observations are aligned and no sources are detected more than once. Additionally, Chandra's pointing accuracy of 0.4 arcsec can be improved either by cross matching the detected sources with those in higher precision catalogues or by cross matching sources with another Chandra observation, which results in relative corrections. This part of the analysis closely follows the guide on "Correcting Absolute Astrometry" (Chandra X-Ray Center, 2022a).

In order to calculate the astrometric shifts, a list of all the sources in the respective observation was generated first by creating an image and then running a source detection tool. The images were obtained with the CIAO tool 'fluximage', which creates exposure

[1] https://cda.harvard.edu/chaser/
[2] https://cxc.cfa.harvard.edu/ciao/download/
[3] https://cxc.cfa.harvard.edu/ciao/index.html

corrected images for a HRC or ACIS observation from the level=2 event file. The energy band was set to the complete HRC-I energy range (0.1-10 keV) with a centre energy of 1.1 keV. A binning parameter of 8 was chosen, which means one pixel corresponds to about 1 arcsec. However, as HRC's energy resolution is rather low, the centre energy value is not as relevant. For the source detection afterwards, the CIAO tool 'wavdetect' was used. Before running 'wavdetect', the a PSF (=Pointspreadfunction) map needed to be created. This was done using the script 'mkpsfmap', which basically looks up the radius of Chandra's PSF for each pixel in a given image at a specific energy, assuming a circular PSF. In this particular case, the energy parameter was again set to 1.1 keV.

Once the source detection is completed, the correction parameters can be determined by cross matching the resulting source list to either the source list of another Chandra observation or to an external catalogue as reference. This was done with the CIAO tool 'wcs_match', which shifts the positions of the sources on the input list to those in the reference file, so that their distances are minimised. As output, the matrix coefficients corresponding to the shift are given:

$$\begin{pmatrix} X' \\ Y' \end{pmatrix} = \begin{pmatrix} a_1 & a_2 \\ a_3 & a_4 \end{pmatrix} \begin{pmatrix} X \\ Y \end{pmatrix} + \begin{pmatrix} t_1 \\ t_2 \end{pmatrix} \tag{12}$$

In Equation 12, X' and Y' describe the shifted source coordinates, while X and Y stand for the original source position. Possible rotation is described by a_1, a_2, a_3, and a_4, translation by t_1 and t_2. One can select, whether the shifting is to include rotation as well as translation or solely translation. In the analysis in this work, the latter method was chosen, which means for the astrometric corrections the parameters t_1 and t_2 were determined for each observation relative to the respective reference. The parameters are calculated in units of physical pixels. One pixel on the HRC-I detector covers 0.13 arcsec, so in order to convert t_1 and t_2 to arcsec, the values were multiplied by 0.13 arcsec.

In an attempt to obtain a higher pointing accuracy, the sources in the first of the 45 observations (ObsID 10683) were cross matched with the USNO-A2.0 catalogue, which is an optical catalogue that contains over 520,000,000 stars[4]. The cross matching resulted in $t_1 = 5.93$ and $t_2 = -2.70$, which translates to $t_1 = 0.77$ arcsec and $t_2 = -0.35$ arcsec. The obtained value for t_1 is quite obviously higher, than Chandra's pointing accuracy of 0.4 arcsec. Figure 12 shows an image obtained with 'fluximage' from the event file of observation 10683 including the detected sources in red and the sources listed in the USNO-A2.0 catalogue in green. It is evident that there are hardly any records of optical sources in the core region of M31, where the majority of the X-ray sources has been detected. This is because of the brightness of the core of M31 in the optical, which makes the detection of individual stars in this area impossible. Therefore, it is likely that the number of matched sources was insufficient to reliably determine the correction parameters or rather that some of the X-ray sources were not matched with

[4] http://tdc-www.harvard.edu/catalogs/ua2.html

their actual optical counterparts. This would explain, why the calculated value for t_1 exceeds the pointing accuracy of Chandra. As the validity of the obtained parameters seems questionable, cross matching the observations with an external catalogue was omitted. It was proceeded with cross matching the observations with each other to align

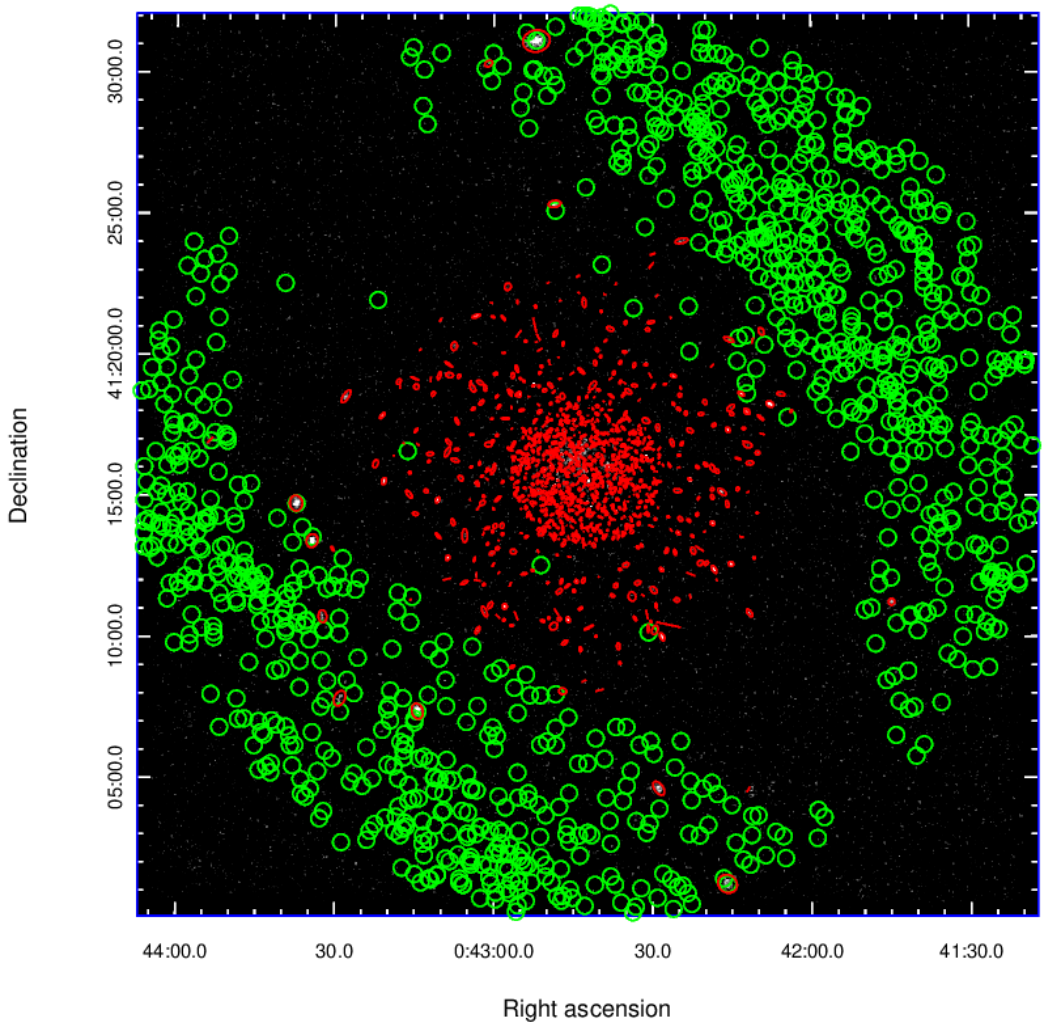

Figure 12: Image created with 'fluximage' from the level=2 event file of observation 10683. The sources detected by 'wavdetect' are marked in red, the sources listed in the USNO-A2.0 catalogue in green. It is evident that hardly any X-ray sources overlap with optical sources listed in the catalogue.

them and improve the pointing in a relative way. For the first attempt, observation 10683 was chosen as reference and t_1 and t_2 were determined for each one of the 44 remaining observations relative to observation 10683. Prior to the source matching, image creation and source detection were executed for all 44 observations in the same way as is described

above. The resulting parameters are visualised in Figure 13. Unfortunately, for 14 of the 44 observations either t_1 or t_2 again exceeds Chandra's pointing accuracy. To improve this result, the reference file was changed from observation 10683 to observation 1912, which has the highest exposure time compared to the rest of the observations. It is assumed that because of the higher statistics, the source positioning of longer observations is better compared to shorter observations. The parameters resulting from the cross matching with observation 1912 are displayed in Figure 14. A slight improvement is evident compared to the results from before, as only 9 instead of 14 values exceed the threshold value of 0.4 arcsec. When looking at the detected sources in the observations with an offset higher than 0.4 arcsec, there is no obvious reason for the shift compared to the observations with values below the threshold value. Therefore, the offsets relative to observation 1912 were applied to all 44 observations, using the CIAO tool 'wcs_update'.

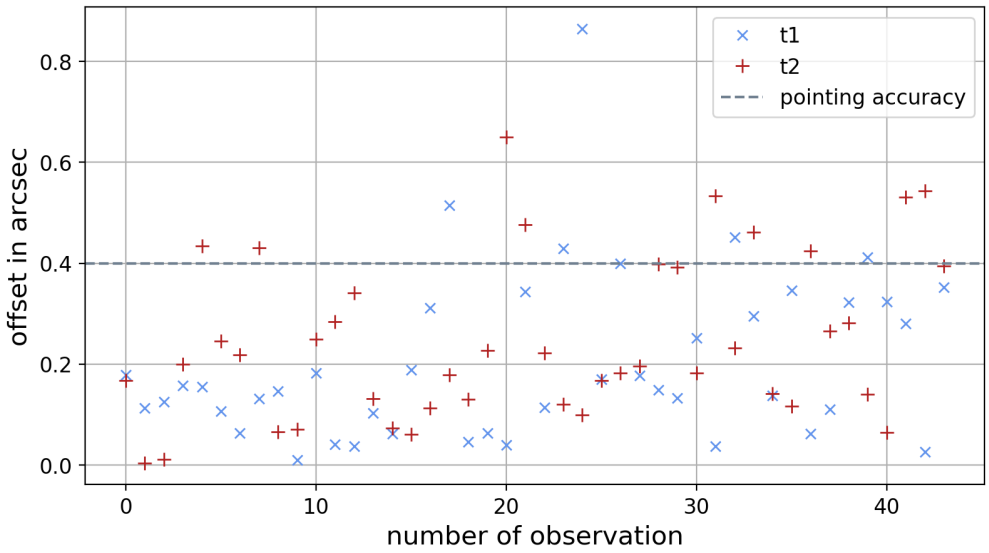

Figure 13: Astrometric correction parameters t_1 (blue crosses) and t_2 (red pluses) in arcsec for all 44 observations relative to observations 10683. The dashed line marks the pointing accuracy of Chandra.

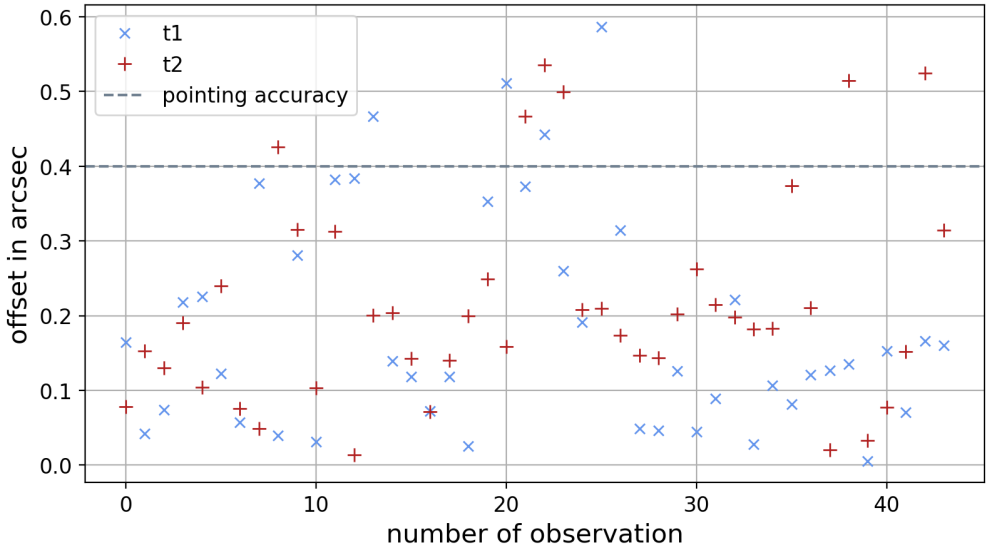

Figure 14: Astrometric correction parameters t_1 (blue crosses) and t_2 (red pluses) in arcsec for all 44 observations relative to observations 1912. The dashed line marks the pointing accuracy of Chandra.

4.2. Merged Images and Upper Limit on Source Flux

After applying astrometric corrections to the data, all 45 observations are effectively aligned so that merging them to obtain stacked images is possible. This was done using the CIAO script 'merge_obs', following the thread 'Using merge_obs to combine observations and create exposure-corrected images' (Chandra X-Ray Center, 2022b). As input, the tool requires the respective corrected level=2 event files and combines them, creating a single merged level=2 event file and exposure corrected images. The binsize was again set to 8. As described in subsection 4.1, the correction parameters relative to observation 1912 exceeded Chandra's pointing accuracy for 9 observations. Therefore, two separate images were created: one using only the remaining 35 observations plus observation 1912 and the other using all 45 observations to achieve better statistics. The resulting images are displayed in Figure 16 and Figure 15. The location of SAnd, as documented in the SIMBAD Astronomical Database[5] (R.A. $00^{\mathrm{h}}42^{\mathrm{m}}43^{\mathrm{s}}.12368$ decl. $+41°16'03''.2124$) is marked by a red cross. The centre of M31 (R.A. $00^{\mathrm{h}}42^{\mathrm{m}}44^{\mathrm{s}}.330$ decl. $+41°16'07''.50$ according to SIMBAD) is marked by a green cross.

Unfortunately, SNR 1885A is not visible in either of the images. However, an upper limit on the source flux could be determined nonetheless. In order to obtain values for the source flux, the upper limit on the count rate at the source location was determined first with the CIAO 'srcflux' script, following the 'Computing the Intensity Upper Limit for an Unresolved Source' thread (Chandra X-Ray Center, 2022d) on the CIAO website.

[5] http://simbad.cds.unistra.fr/simbad/

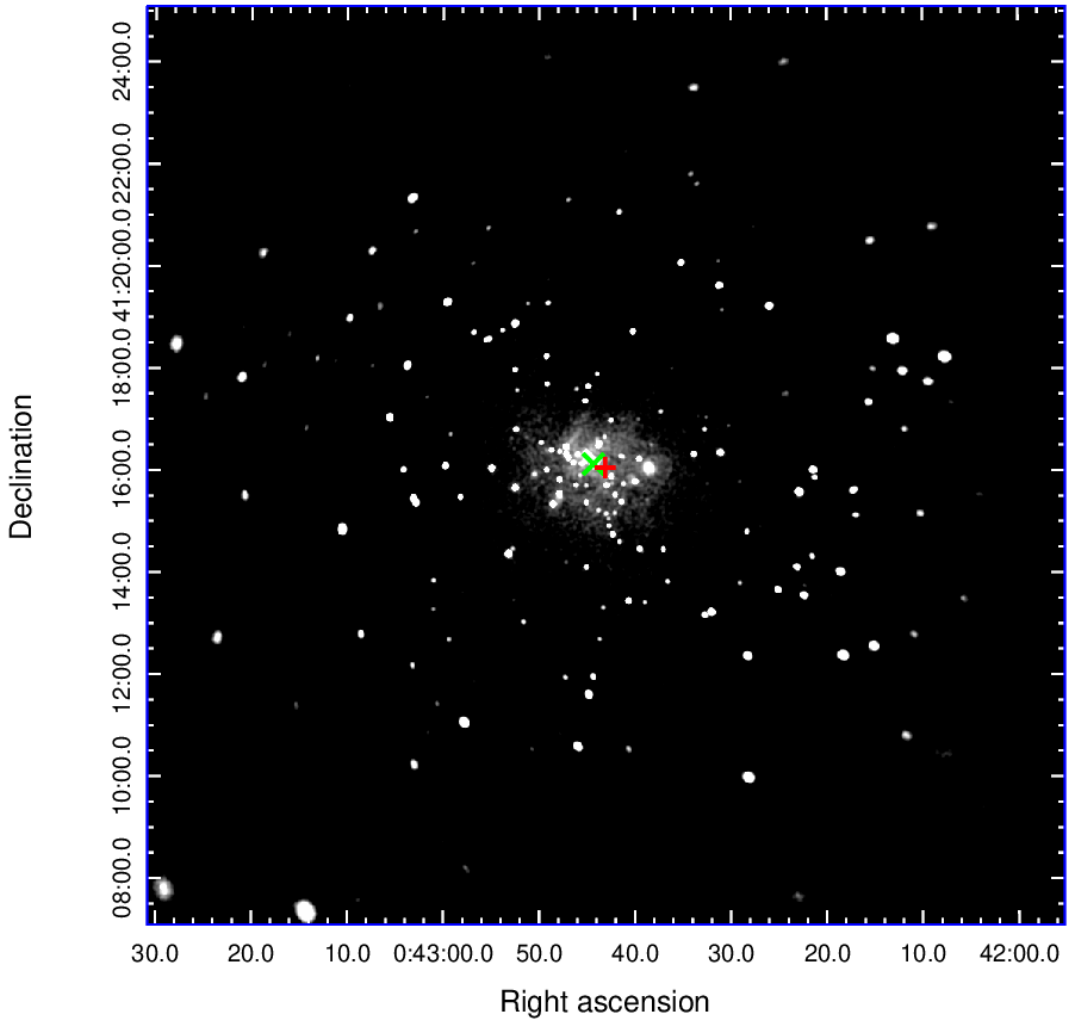

Figure 15: Merged image of the central region of M31, created from 36 Chandra HRC-I data sets. The red cross marks the reported position of SAnd and the green cross indicates the centre of M31. For this image binsize=8 was chosen. One pixel corresponds to ≈ 1 arcsec.

The 'srcflux' tool calculates net count rates and fluxes including uncertainties from the level=2 event files for a specified source location and region, background region and energy band. If multiple files are given as input, the merged count rate is calculated automatically, provided that CIAO version 4.13 or newer is used. For that reason, the rest of the analysis was done with CIAO version 4.14 instead of version 4.12, like previously.

In a first attempt to determine an upper limit for the count rate, only the location of SAnd was given and the default settings were used for source and background regions.

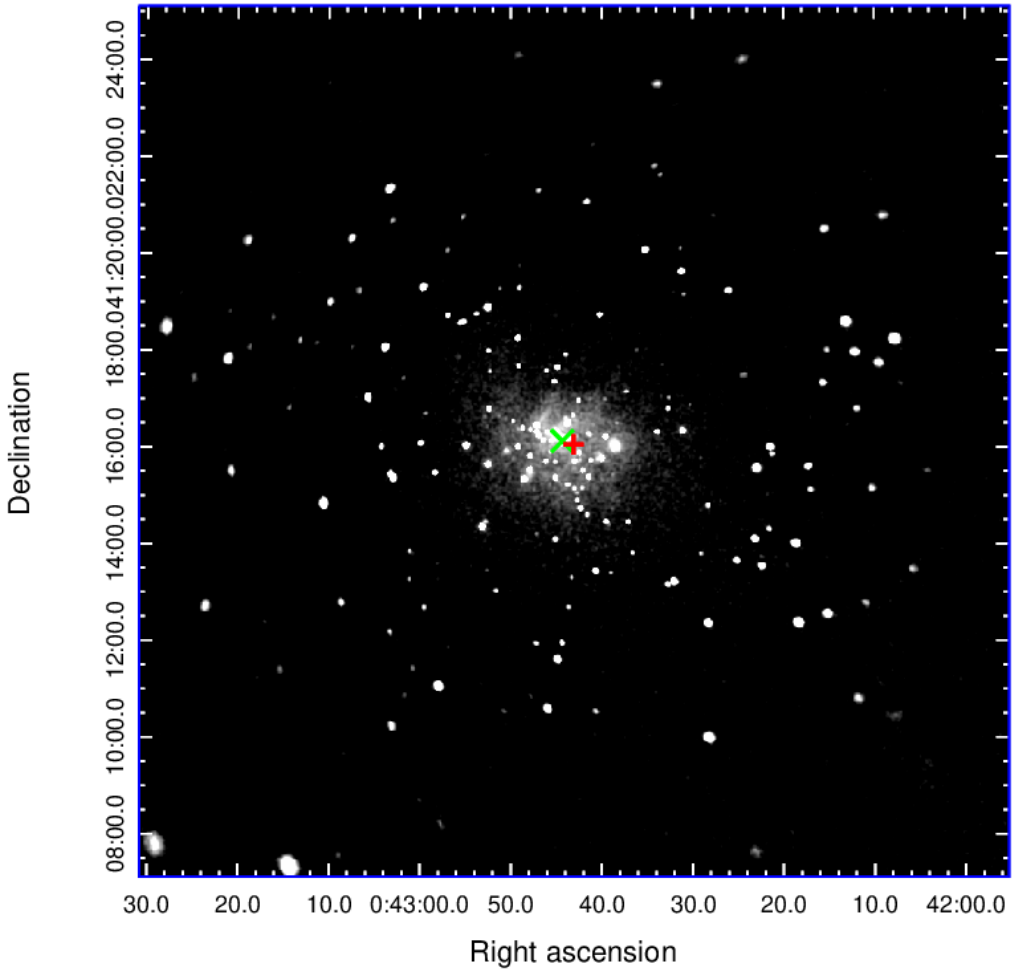

Figure 16: Merged image of the central region of M31, created by merging all 45 Chandra HRC-I data sets. The red cross marks the reported position of SAnd and the green cross indicates the centre of M31. For this image binsize=8 was chosen. One pixel corresponds to ≈ 1 arcsec.

If not specified, 'srcflux' defines a circle enclosing 90% of Chandra's PSF as source region, which in this case corresponds to roughly 0.83 arcsec. As background region, an annulus with an inner radius equal to the radius of the source region and an outer radius of five times the radius of the source region (~ 4.17 arcsec) is assumed. Both source and background regions are centred at the respective source position.

Evidently, background and source region are joined in the default settings. Therefore, to ensure no source counts are assigned to the background region, the upper limit

for the count rate was determined a second time using an annulus with an inner radius of three times that of the source region (~ 2.5 arcsec) as new background region. The outer radius and the source region itself were not altered. Both background and source regions are displayed in Figure 17 and Figure 18. The energy band parameter was set to the full range of HRC-I (0.1-10 keV) in both cases. For the same reason as explained above, the upper limit on the count rate was calculated twice in every attempt: once using only 36 observations and once for all 45 observations. Running 'srcflux' with the listed input parameters results in the values given in the second columns of Table 1 and Table 2.

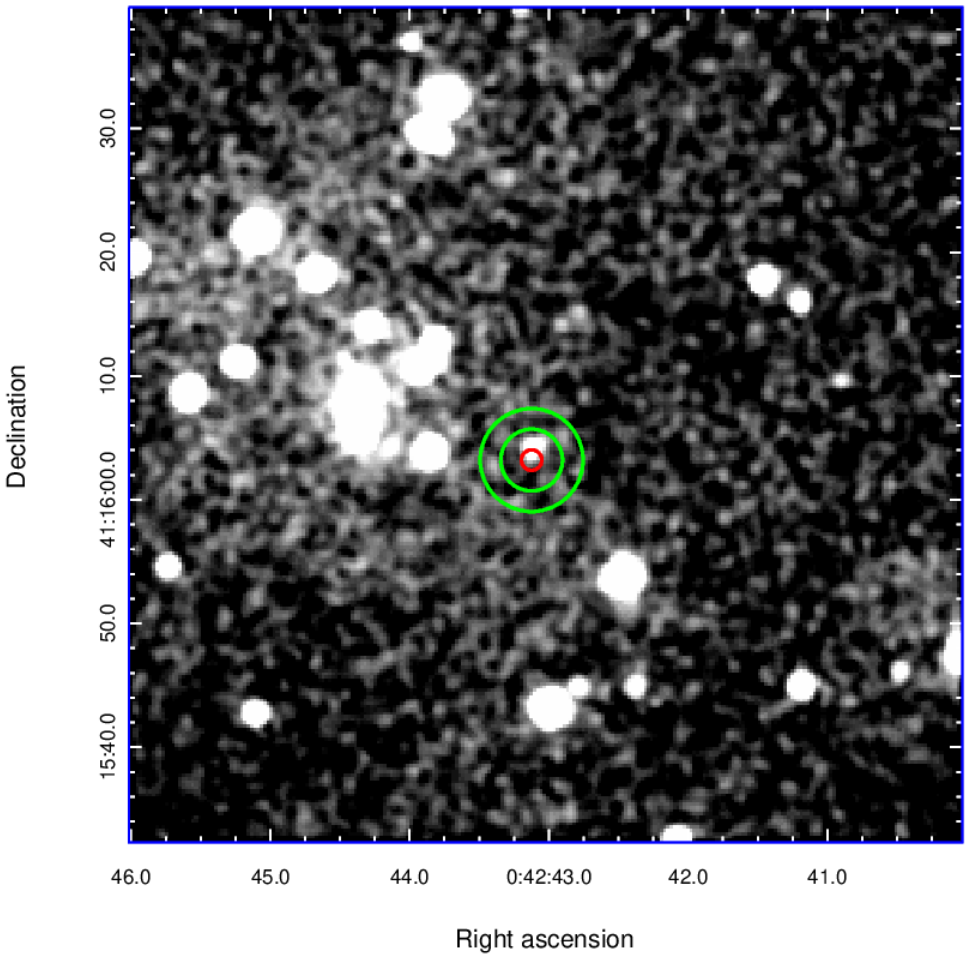

Figure 17: Image section of Figure 15 showing source and background regions to determine the upper limit on the source flux of SNR1885. The source region is indicated by the red circle ($R = 0.833$ arcsec) and the background region by the green annulus ($R_{inner} \approx 2.5$ arcsec, $R_{outer} \approx 4.2$ arcsec). For this image binsize=2 was chosen. One pixel corresponds to about 0.26 arcsec.

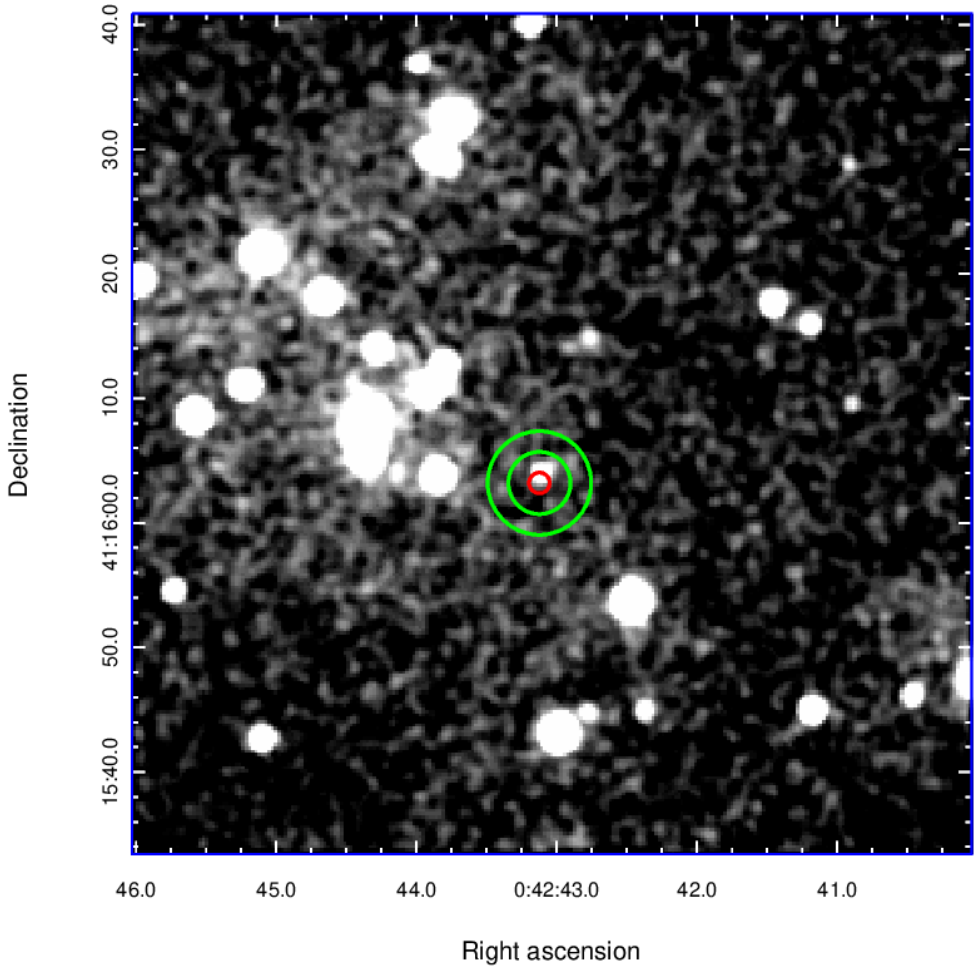

Figure 18: Image section of Figure 16 showing source and background regions to determined the upper limit on the source flux of SNR1885. The source region is indicated by the red circle ($R = 0.833$ arcsec) and the background region by the green annulus ($R_{inner} = 2.5$ arcsec, $R_{outer} = 4.17$ arcsec). For this image binsize=2 was chosen. One pixel corresponds to about 0.26 arcsec.

To obtain the upper limit on the source flux, the count rates needed to be converted to units of erg cm^{-2}s^{-1}. This was done using WebPIMMS[6], an online mission count rate simulator provided by NASA's High Energy Astrophysics Science Archive Research Centre (HEASARC) for that exact purpose. The tool calculates the flux for a specified energy range and mission specific detector, in this case Chandra's HRC-I, from the measured count rate, assuming a given source model. The energy range was set to

[6] https://heasarc.gsfc.nasa.gov/cgi-bin/Tools/w3pimms/w3pimms.pl

0.1-10 keV to match that of HRC-I and an APEC model at a temperature of 1 keV and solar element abundances were assumed. The redshift was set to none. To consider absorption by gas in the Milky Way, the galactic column density at the position of M31 was adopted, which amounts to $7 \times 10^{20}\,\mathrm{cm}^{-2}$ (Sasaki et al., 2012). As SNR 1885A is located in the central region of the Andromeda Galaxy, absorption by the gas in M31 is also expected, which is taken into account by setting the intrinsic column density to $1 \times 10^{21}\,\mathrm{cm}^{-2}$ (Sasaki et al., 2012). The resulting flux values are displayed in the second columns of Table 1 and Table 2. Additionally, the corresponding X-Ray luminosities for the flux values in Table 2 were calculated to better be able to compare the luminosity with that of other SNRs in the following chapter. Luminosity L and source flux f are connected via $L = f\pi d^2$, where d is the distance to the respective object. In this case, a distance of $d = 780\,\mathrm{kpc}$ to M31 was assumed like in Kaaret (2002). The resulting values are given in the third column of Table 2.

# observations	upper limit count rate in counts s^{-1}	upper limit source flux in erg $\mathrm{cm}^{-2}\mathrm{s}^{-1}$
36	9.58×10^{-5}	9.35×10^{-16}
45	8.59×10^{-5}	8.40×10^{-16}

Table 1: Calculated upper limits for count rate and source flux at the position of SNR 1885A ('srcflux' default settings).

# observations	upper limit count rate in counts s^{-1}	upper limit source flux in erg $\mathrm{cm}^{-2}\mathrm{s}^{-1}$	upper limit luminosity in erg s^{-1}
36	9.98×10^{-5}	9.75×10^{-16}	1.53×10^{34}
45	8.88×10^{-5}	8.67×10^{-16}	1.36×10^{34}

Table 2: Calculated upper limits for count rate and source flux at the position of SNR 1885A (specified source and background regions).

4.3. Comparison to other SNRs

In order to contextualise the obtained upper limit on the X-ray source flux of SNR1885, it is compared to X-ray fluxes of other SNRs within the Milky Way and in M31. Figure 19 shows the X-ray luminosities in the 0.3-8 keV-band of some of the known younger Galactic remnants (type I and type II respectively) along with the upper limit on the luminosity of SNR1885 (see Table 2). Additionally, the plot contains the reconstructed X-ray light-curves of four of the oldest known X-ray SNe, SN1970G, SN1968D, SN1957D and SN1941. The plotted luminosities and ages of the younger Galactic remnants are given in Table 4, for the X-ray SNe see subsection B.3. Figure 19 can be found in a publication by Ramakrishnan and Dwarkadas (2020). They presented a study of the evolution of the oldest known X-ray core collapse SNe by reconstructing their light curves over a few decades and drew comparisons to the X-ray emission of known Galactic SNRs

with ages of up to over two thousand years. For the purpose of this work, the upper limit on the luminosity of SNR1885 obtained from merging all 45 observations (see Table 2) has been added to the original plot, as well as two power law fits following Equation 6 and Equation 10, which will be discussed in detail further down.

Evidently, the X-ray luminosities of most of the Galactic remnants as well as of the four X-ray SNe exceed the upper limit of SNR1885 by two to three orders of magnitude, although the value lies within the error range of two data points from SN1970G and SN1968D. Exceptions are the remnant of the type II-supernova SN1181 and the remnants of SN1006 and G1.9 + 0.3, which are both classified as type Ia.

Generally, the luminosity seems to initially decrease with time. This result was also found in the analysis by Ramakrishnan and Dwarkadas (2020). The luminosity of G1.9 + 0.3 and the upper limit for SNR1885 fit into this decreasing pattern. Among the younger Galactic remnants the opposite is the case and the luminosity seems to rise with time. As previously shown in subsection 2.3, the initial decrease of X-ray emission from SNRs is expected according to the self-similar solution. In this stage, the evolution of the remnant is believed to largely be dominated by the ejecta. In theory, the X-ray luminosity is expected to evolve as follows (see Equation 6) (Ramakrishnan and Dwarkadas, 2020):

$$L_X = A_1\, t^{-[(2s-3)n+12-7s]/(n-s)} \text{ for } T_e > 2.24\,\text{keV} \tag{13}$$

However, once the remnant transitions to the Sedov-Taylor phase, as the forward shock propagates further and sweeps up the surrounding ISM and the reverse shock reaches the centre of the remnant and dissipates, the X-ray luminosity is predicted to rise again. In the ST-phase, L_X is expected to evolve as given by Equation 10 (Ramakrishnan and Dwarkadas, 2020):

$$L_X = A_2\, t^{(8.88-4.96s)/(5-s)} \tag{14}$$

Subsequently, the theoretical considerations are largely consistent with the data, if it is assumed that most of the younger remnants have begun transitioning to the ST-phase. This assumption is rather realistic, if one takes a look at research results on some of the younger remnants. For example, extensive observations of Tycho's SNR with Chandra and XMM Newton have revealed the distribution of the shocked matter and the exact positions of forward shock, reverse shock and contact discontinuity could be determined. Model calculations show that the ejecta are no longer expanding freely and the remnant has started transitioning into the ST-phase (Seward and Charles, 2010).

To further investigate the correlation of the theoretical predictions to the actual luminosities, especially with regard to the obtained upper limit for SNR1885, Equation 13 was used to fit the data of the old X-ray SNe, including the remnant of the type Ia-SN G1.9+0.3 and SNR1885. SN1941C was left out, as there is only data from one observation available (Ramakrishnan and Dwarkadas, 2020). An electron temperature $T_e > 2.24\,\text{keV}$ was assumed, because the steeper decline is in better agreement with the data than it is the case for $T_e \leq 2.24\,\text{keV}$ (see Figure 3). As explained in subsection 2.3, the power-law

index n determines the density profile of the ejecta and lies typically in the range of $9 < n < 11$ for stellar envelopes. Therefore, $n = 10$ was chosen here. The index s characterises the density of the CSM. The self similar solution only holds for $s < 3$ and $s = 2$ would imply a steady wind. To match the decline of the plotted luminosites, an index n close to $n = 3$ had to be selected. For a steady wind, the slope was not steep enough to describe the actual data. As $s = 3$ cannot be chosen, for the fit in Figure 19, the index was set to $s = 2.99$. This implies that the density of the CSM decreases more rapidly than would be the case for a steady wind. If these values for n and s are inserted into Equation 13, we obtain $L_X = A_1\, t^{-2.98}$, which was then fit to the data. The resulting value for the fit parameter A_1 can be found in Table 3.

Even though both G1.9+0.3 and SNR1885 are still fainter than predicted by the fit, the data are well in agreement with the theory. The fit suggests that once the X-ray SNe have reached the age of SN1885, their luminosities will be around the same order of magnitude as the current upper limit of SNR1885. However, one has to keep in mind that the SNe discussed in Ramakrishnan and Dwarkadas (2020) were classified as type II, while SAnd is believed to have been a type Ia-SN (see subsection 3.2). This may account for differences in the in the evolution of L_X.

Equation 14 was used to fit the data of the Galactic remnants. Merely SN1006 and SN1181 were excluded from the fit. G1.9+0.3 was also left out, as it was already included in the previous fit. Here, the index s was set to $s = 0$, as the forward shock is now expected to propagate into ISM with such a density profile (Ramakrishnan and Dwarkadas, 2020). Inserting the parameters into Equation 14 results in $L_X = A_1\, t^{-2.98}$. The fit parameter A_2 is given in Table 3. Evidently, the data also agree with the theoretical predictions. The only exceptions are the remnants of SN1006 and SN1181, which are distinctly fainter than the rest of the Galactic remnants. The reason is the position of the remnants within the Galaxy. SN1006 is located about 15° above the galactic plane (Seward and Charles, 2010) , which means the density of the surrounding medium is fairly low. The forward shock is bound to eventually run out of matter to sweep up, which in turn results in a lower X-ray luminosity. The same reasoning can be applied to SN1181 (Ramakrishnan and Dwarkadas, 2020), which is why both remnants were excluded from the fit.

When comparing the X-ray flux of SNR1885 to that of other SNRs, one also needs to consider absorption. G1.9+0.3 is with an age of 100 yrs the youngest known Galactic SNR. Its measured X-ray luminosity is comparable to the upper limit on SNR1885. G1.9+0.3 is located at a distance of approximately 8.5 kpc near the Galactic centre, where absorption is relatively high (absorbing column density of $5.5 \times 10^{22}\,\mathrm{cm}^{-2}$), accounting for a lower detected luminosity (Reynolds et al., 2008). SNR1885 and G1.9+0.3 are with 127 and 100 yrs fairly close in age. If SNR1885 is placed close to the centre of M31, strong absorption would be a valid reason for the lack of X-ray emission from SNR1885, much like it is the case for G1.9+0.3.

Finally, if SNR1885 is compared to fluxes of other SNRs in M31, one finds that the

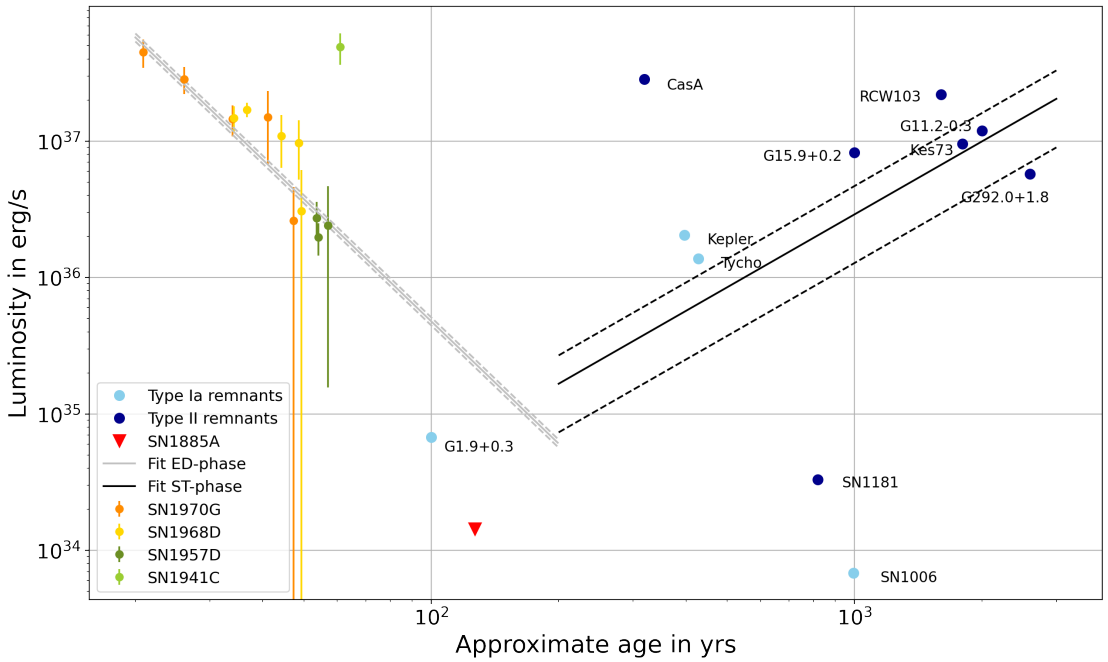

Figure 19: X-ray luminosities of the oldest known X-ray SNe and some younger galactic remnants. The original plot is from Ramakrishnan and Dwarkadas (2020). The upper limit on the luminosity of SNR1885 (45 observations) was added to the plot, as well as the two fits for ED-phase (grey) and ST-phase (black) using Equation 13 and Equation 14. The dashed lines mark the error ranges of the parameter $A_{1/2}$ determined by the fit.

A_1 in $\mathrm{erg\,s^{-1}}$ (ED-phase)	A_2 in $\mathrm{erg\,s^{-1}}$ (ST-phase)
$(4.30 \pm 0.29) \times 10^{41}$	$(1.4 \pm 0.8) \times 10^{31}$

Table 3: Fit-parameter $A_{1/2}$ for both fits in Figure 19.

obtained upper limit is by at least one order of magnitude lower, than the luminosities of other remnants. Sasaki et al. (2012) presented a study of SNRs in M31 detected by XMM Newton in 2012. In total, 26 X-ray sources were classified as SNRs and catalogued. The determined luminosities in the 0.35-2.0 keV band range from $2.1 \times 10^{35}\,\mathrm{erg\,s^{-1}}$ to $3.1 \times 10^{36}\,\mathrm{erg\,s^{-1}}$, so one to two orders of magnitude higher than the upper limit for SNR1885, which is quite similar to the comparison to the younger Galactic remnants.

All in all, one can assume that the evolution of SNR1885 is still largely dominated by the ejecta and the remnant has not yet fully transitioned to the ST-phase, which could explain why it is not strongly emitting in X-rays. This is also in agreement with optical observations, stating that the ejecta are expanding freely (see subsubsection 3.3.1). There

remnant	age in yrs	luminosity in $10^{36}\,\mathrm{erg\,s^{-1}}$
Tycho	428	1.37
SN1006	994	6.84×10^{-3}
G1.9+0.3	100	6.74×10^{-2}
Kepler	396	2.04
CasA	319	28.4
SN1181	819	3.30×10^{-2}
G292.0+1.8	2600	5.73
G15.9+0.2	1000	8.24
Kes73	1800	9.53
RCW103	1600	22.0
G11.2-0.3	2000	11.9
SAnd	127	1.36×10^{-2}

Table 4: Age and luminosity (from Chandra SNR catalogue: https://hea-www.harvard.edu/ChandraSNR/index.html) for the in Figure 19 displayed SNRs. (Ramakrishnan and Dwarkadas, 2020)

is a possibility that as soon as SNR1885 transitions into the ST-phase, X-ray emission will increase to a point, where the remnant will be detectable. However, if SNR1885 is located close to the centre of M31, strong absorption by the surrounding medium would also contribute to prevent the detection of potential X-ray emission, much like it is the case for G1.9+0.3 placed near the Galactic centre. When comparing SNR1885 and G1.9+0.3, one finds that those are the only two remnants nearing the end of the ED-phase and as already mentioned above, both objects are considerably fainter in X-rays than predicted by theory in the ED-phase (see Figure 19). This might indicate that the X-ray luminosity declines at a higher rate than implied by the fit in the second half of the ED-phase. One last imaginable scenario to explain the absence of X-ray emission from SNR1885 would be if the remnant was located in the halo outside of the galactic plane of M31. Then the density of the surrounding medium swept up by the forward shock would be very low, which reduces X-ray emission like it is the case for the remnant of SN1006.

4.4. Source near SNR1885

Despite SNR1885 not being visible in the images, another X-ray source close to the position of SAnd could be detected. This is not surprising, as this source had been identified for the first time by Kaaret (2002) and his observation (ObsID 1912) was included in the 45 data sets processed in this work. The source was listed as CXOM31 J004243.1+411604 and positioned at R.A. $00^{\mathrm{h}}42^{\mathrm{m}}43^{\mathrm{s}}.11$ decl. $+41°16'04''.2$. The measured luminosity amounts to $2.9 \times 10^{36}\,\mathrm{erg\,cm^{-2}s^{-1}}$ (Kaaret, 2002).

Comparing the X-ray data to HST images showing the optical absorption feature of SNR1885 led Kaaret (2002) to the conclusion that the source is not the X-ray counterpart to SNR1885, as the angular distance to the centre of the absorption feature seems to be about 1.3 arcsec. Further examination of HST observations revealed a bright point source within 0.15 arcsec of the position of the X-ray source. Based on the estimated flux of $3.5 \times 10^{-16}\,\mathrm{erg\,cm^{-2}s^{-1}\AA^{-1}}$ obtained by analysing the HST observations, Kaaret (2002) suspected the source to be an optical nova. Hofmann et al. (2013) published a catalogue of X-ray sources in the central region of M31. The catalogue is based on the Analysis of Chandra HRC-I data, also including the observation discussed in Kaaret (2002). The X-ray source was classified as a classical nova here as well.

A classical nova (CNe) is a one-time eruption, resulting in temporary increase of brightness of a star between 9 and 16 magnitudes (Griffiths, 2018). Following the eruption, the star's luminosity typically reaches values in the order of $10^4\,\mathrm{L_\odot}$ (Bode, 2010). This state can last from a few days up to several years, depending on the brightness of the explosion. Generally, it can be stated that brighter novae fade faster. After a nova outburst, the star will go back to its level of brightness prior to the explosion, which usually lies in the order of $\mathrm{L_\odot}$ (Bode, 2010; Griffiths, 2018).

CNe occur in close binary systems, which consist of a CO- or NeO-type WD primary and a low mass main sequence secondary, orbiting each other (Bode, 2010). The orbital period of such a system usually amounts to less than 12 hours, its size is comparable to the Earth-Moon system (Goddard Space Flight Center, 2010). Due to the strong gravitational force of the WD and the short distance to its main sequence companion, hydrogen-rich material from the main sequence star is accreted onto the surface of the WD at rates in the order of $\dot{\mathrm{M}} \approx 10^{-9}\,\mathrm{M_\odot yr^{-1}}$ (Bode, 2010; Griffiths, 2018). As the electrons in the degenerate matter of the WD are only kept apart by the degeneracy pressure, increase in matter forces the electrons to higher energy levels. This means pressure and temperature increase. At a sufficient amount of accreted material, this results in hydrogen burning, starting with the proton proton-chain. The fusion of hydrogen to helium corresponds to a release of energy, which causes the temperature to rise further until the CNO-cycle is initiated (at $T = 2 \cdot 10^6\,\mathrm{K}$). Due to the fact that the degeneracy pressure is independent of the temperature, those reactions result in thermonuclear runaway (TNR). As soon as the gas pressure becomes higher than the degeneracy pressure, the outer layers expand rapidly, leading to the nova explosion (Sasaki, 2020).

A few of these sources have been detected in supersoft X-rays before. They usually have black body spectra with temperatures between 15 eV and 80 eV (Kahabka and van den Heuvel, 1997). In Kaaret (2002), the unabsorbed source luminosity was calculated from the HRC-I count rate over an energy range of 0.1-10 keV, assuming a black body spectrum at 80 eV. Kaaret (2002) gives a resulting unabsorbed luminosity of $9 \times 10^{36}\,\mathrm{erg\,s^{-1}}$. The source flux of the nova was determined the same way as described in subsection 4.2 for both 36 and all 45 observations using 'srcflux'. Source and background region were

again chosen to be a circle enclosing 90% of Chandra's PSF and an annulus with an inner radius of three times and an outer radius of five times that of the source region (see Figure 20). Both source and background region were centred on the given source location. The resulting count rate values can be found in the first column of Table 5. The count rates were converted to flux values using WebPIMMS[7] with the same parameters as before with the exception of the source model. In this case, a blackbody spectrum was chosen with a temperature of 80 eV, just like in Kaaret (2002). From the source flux, the luminosity was calculated, assuming a distance of 780 kpc to M31. The results are displayed in the second and third column of Table 5. Compared to the luminosity determined in Kaaret (2002) ($2.9 \times 10^{36}\,\mathrm{erg\,cm^{-2}s^{-1}}$), the values in this work are by two orders of magnitude lower. This is reasonable, because for multiple observations, the merged count rates are calculated from the sum of source and background counts and then weighted by the exposure (Chandra X-Ray Center, 2022c). If the source is not visible in all observations, this will result in a lower count rate, and subsequently in a lower source flux, than if only one single observation is used.

It is also important to mention that as the X-ray source and SNR1885 lie very close together, the source regions chosen to determine the count rates and subsequently the X-ray fluxes and luminosities of the two objects inevitably overlap. Therefore, it is likely that emission originating from the X-ray source nearby contributed to the obtained upper limit for SNR1885, especially since the values for the luminosities are in the same order of magnitude (see Table 2 and Table 5).

# observations	count rate in $\mathrm{cnts\,s^{-1}}$	source flux in $\mathrm{erg\,cm^{-2}s^{-1}}$	luminosity in $\mathrm{erg\,s^{-1}}$
36	$(2.0 \pm 0.4) \times 10^{-4}$	$(2.3 \pm 0.5) \times 10^{-15}$	$(4.2 \pm 0.9) \times 10^{34}$
45	$(1.69 \pm 0.30) \times 10^{-4}$	$(2.0 \pm 0.4) \times 10^{-15}$	$(3.6 \pm 0.7) \times 10^{34}$

Table 5: Calculated count rates and source fluxes at the position of the X-ray source near SAnd.

[7] https://heasarc.gsfc.nasa.gov/cgi-bin/Tools/w3pimms/w3pimms.pl

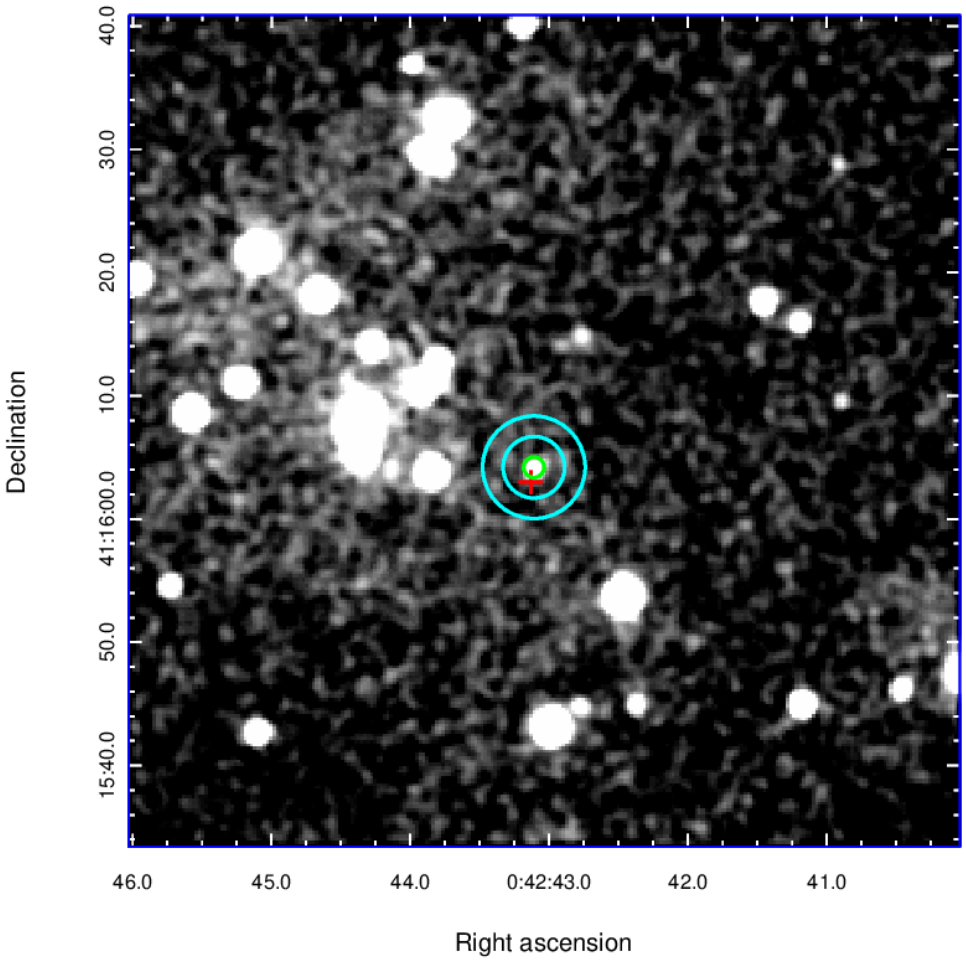

Figure 20: Image section of Figure 16 showing source and background regions to determined the source flux of the Chandra source near SAnd. The source region is indicated by the green circle ($R = 0.833$ arcsec and the background region by the cyan annulus ($R_{inner} = 2.5$ arcsec), $R_{outer} = 4.17$ arcsec). The red cross marks the position of SAnd. For this image binsize=2 was chosen. One pixel corresponds to about 0.26 arcsec.

5. Conclusion

In this work potential X-ray emission from the remnant of the historical SN SAnd in M31 was investigated using Chandra HRC-I data. Prior to the data analysis, a overview of the history of SAnd and of previous observations of its remnant was given.

SAnd was discovered by the German astronomer Ernst Hartwig on 20 August 1885 with the great refractor at the observatory in Dorpat, Estonia. The public announcement about the discovery of SAnd followed on 31 August 1885 (Jones, 1976). SAnd is generally classified as a type Ia-SN mainly based on its spectral features (de Vaucouleurs and Corwin, 1985; Graham, 1988). However, reconstructions of the light curve of the event showed that SAnd was sub-luminous and had one of the fastest light curves ever observed (de Vaucouleurs and Corwin, 1985), which is why the classification as type Ia was questioned by multiple sources and the possibility of SN1885A belonging to some other sub-type of type I-SNe has been suggested (Chevalier and Plait, 1988; van den Bergh, 2002).

The remnant of SAnd remained undetected for over 100 years and was discovered by Fesen et al. (1989) with the ground based telescope at Kitt Peak National Observatory in Arizona in Fe I absorption images. More detailed follow up studies with the Hubble Space Telescope revealed that the remnant showed in Ca I, Ca II, Fe I as well as Fe II (Fesen et al., 2007). Radio observations with the VLA allowed to determine an upper limit on the radio luminosity of $1 \times 10^{23}\,\mathrm{erg\,s^{-1}\,Hz^{-1}}$ at 6 cm (Dickel and Dodorico, 1984). Thus far, no X-ray emission from the remnant has been detected, although observations of the central region of M31 with the Chandra X-ray observatory by Kaaret (2002) revealed a X-ray source within 1.3 arcsec of the location of SAnd. This source, however, has been identified as an optical nova and is independent of SAnd (Kaaret, 2002).

In this work, an upper limit on the X-ray flux of SNR1885 was determined by combining a total of 45 Chandra HRC-I observations. After applying astrometric corrections to the data, two merged images were created: one image using all 45 observations and one image using 36 observations for which the obtained astrometric corrections did not exceed Chandra's pointing accuracy of 0.4 arcsec. Unfortunately, the remnant was not visible in either of the images but an upper limit on the source flux for each image was calculated. The resulting values for the upper limit are $9.75 \times 10^{-16}\,\mathrm{erg\,cm^{-2}s^{-1}}$ (0.1-10 keV band, 36 observations) and $8.67 \times 10^{-16}\,\mathrm{erg\,cm^{-2}s^{-1}}$ (0.1-10 keV band, 45 observations). This corresponds to X-ray luminosities of $1.53 \times 10^{34}\,\mathrm{erg\,s^{-1}}$ (36 observations) and $1.36 \times 10^{34}\,\mathrm{erg\,s^{-1}}$ (45 observations) assuming a distance of 780 kpc to M31. Additionally, the X-ray luminosity of the Chandra source near the location of SAnd, identified by Kaaret (2002) as an optical nova, was determined. The results for both images are $(4.2 \pm 0.9) \times 10^{34}\,\mathrm{erg\,s^{-1}}$ (36 observations) and $(3.6 \pm 0.7) \times 10^{34}\,\mathrm{erg\,s^{-1}}$ (45 observations). It is noted that as the two objects are so close together, the flux of the Chandra source might have contributed to the upper limit on the flux of SNR1885.

Comparison of the obtained upper limit on the X-ray luminosity of SNR1885 from combining all 45 observations to the measured X-ray luminosities of known Galactic remnants shows that the value is almost two orders of magnitude lower. The same result is found when comparing the upper limit to the luminosities of SNRs in M31 determined by Sasaki et al. (2012). Nevertheless, the obtained upper limit on the luminosity of SNR1885 is in agreement with theoretical predictions, if one assumes that the remnant is still in the ED-phase, where the X-ray emission is initially expected to decline (Ramakrishnan and Dwarkadas, 2020). It is possible that as SNR1885 begins to transition to the ST-phase, X-ray emission will rise similar to those of the examined Galactic remnants. Moreover, if SNR1885 is located near the Galactic centre, strong absorption could be a reason for the lack of X-ray emission. Another possibility is that SNR1885 is located in the halo of M31, where the ISM density is low. This means the shock would eventually run out of material to sweep up, which would result in lower X-ray emission. Additionally, it was found that the X-ray luminosity might decrease faster towards the end of the ED-phase compared to the beginning.

All in all, only further observations will show how SNR1885 evolves. If the X-ray emission indeed rises to a point where the remnant is detectable, new insights on the evolution of young SNRs and specifically on the end of the ED-phase and the beginning of the transition to the ST-phase could be gained from more detailed observations. Furthermore, valuable information with regard to the classification of SAnd and about type I-SNe in general could be revealed. What remains to say is that SAnd, at the time of its discovery by Hartwig as well as now, really is "[one of] the most fascinating event[s] of modern astronomy" (Jones, 1976).

References

M. F. Bode. The outbursts of classical and recurrent novae. *Astronomische Nachrichten*, 331(2):160, Feb. 2010. doi: 10.1002/asna.200911319.

Chandra IPI Teams. ACIS: Advanced CCD Imaging Spectrometer, 2022a. https://cxc.harvard.edu/proposer/POG/html/chap6.html [Accessed: 2022-05-30].

Chandra IPI Teams. HRC: High Resolution Camera, 2022b. https://cxc.harvard.edu/proposer/POG/html/chap7.html [Accessed: 2022-05-30].

Chandra IPI Teams. High Resolution Mirror Assembly (HRMA), 2022c. https://cxc.harvard.edu/proposer/POG/html/chap4.html [Accessed: 2022-05-30].

Chandra IPI Teams. Mission Overview, 2022d. https://cxc.harvard.edu/proposer/POG/html/chap1.html [Accessed: 2022-05-30].

Chandra X-Ray Center. Correcting absolute astrometry, 2022a. https://cxc.cfa.harvard.edu/ciao/threads/reproject_aspect/ [Accessed: 2022-06-06].

Chandra X-Ray Center. Using merge_obs to combine observations and create exposure-corrected images, 2022b. https://cxc.cfa.harvard.edu/ciao/threads/merge_all/ [Accessed: 2022-06-07].

Chandra X-Ray Center. AHELP for CIAO 4.14: srcflux, 2022c. https://cxc.cfa.harvard.edu/ciao/ahelp/srcflux.html [Accessed: 2022-06-27].

Chandra X-Ray Center. Computing the intensity upper limit for an unresolved source, 2022d. https://cxc.cfa.harvard.edu/ciao/threads/upperlimit/ [Accessed: 2022-06-07].

R. A. Chevalier. Self-similar solutions for the interaction of stellar ejecta with an external medium. *Astrophysical Journal*, 258:790–797, July 1982. doi: 10.1086/160126.

R. A. Chevalier and C. Fransson. Thermal and Non-thermal Emission from Circumstellar Interaction. In A. W. Alsabti and P. Murdin, editors, *Handbook of Supernovae*, pages 875–937. Springer International Publishing, Cham, 2017. ISBN 978-3-319-21846-5. doi: 10.1007/978-3-319-21846-5_34. URL https://doi.org/10.1007/978-3-319-21846-5_34.

R. A. Chevalier and P. C. Plait. The Nature of S Andromedae (SN 1885A). *Astrophysical Journal, Letters*, 331:L109, Aug. 1988. doi: 10.1086/185246.

G. de Vaucouleurs and J. Corwin, H. G. S Andromedae 1885: A Centennial Review. *Astrophysical Journal*, 295:287, Aug. 1985. doi: 10.1086/163374.

J. R. Dickel and S. Dodorico. Radio emission from supernova remnants in M 31 at a wavelength of 6 cm. *Monthly Notices of the RAS*, 206:351–358, Jan. 1984. doi: 10.1093/mnras/206.2.351.

ESA/Hubble. Stellar Wind, 2022. `https://esahubble.org/wordbank/stellar-wind/` [Accessed: 2022-06-20].

R. A. Fesen, A. J. S. Hamilton, and J. M. Saken. Discovery of the Remnant of S Andromedae (SN 1885) in M31. *Astrophysical Journal, Letters*, 341:L55, June 1989. doi: 10.1086/185456.

R. A. Fesen, C. L. Gerardy, K. M. McLin, and A. J. S. Hamilton. Hubble Space Telescope Images and Spectra of the Remnant of SN 1885 in M31. *Astrophysical Journal*, 514(1): 195–201, Mar. 1999. doi: 10.1086/306938.

R. A. Fesen, P. A. Höflich, A. J. S. Hamilton, M. C. Hammell, C. L. Gerardy, A. M. Khokhlov, and J. C. Wheeler. The Chemical Distribution in a Subluminous Type Ia Supernova: Hubble Space Telescope Images of the SN 1885 Remnant. *Astrophysical Journal*, 658(1):396–409, Mar. 2007. doi: 10.1086/510998.

C. P. Gaposchkin. On the Spectrum of the Supernova S Andromedae. *Astrophysical Journal*, 83:245, Apr. 1936. doi: 10.1086/143721.

S. Gaposchkin. The Elusive Maximum of S Andromedae. *Sky and Telescope*, 21:326, June 1961.

Goddard Space Flight Center. Cataclysmic Variables, 2010. `https://imagine.gsfc.nasa.gov/science/objects/cataclysmic_variables.html` [Accessed: 2022-06-21].

J. R. Graham. SN 1984A and S Andromedae: Two Examples of Rare Type IA Supernovae. *Astrophysical Journal, Letters*, 326:L51, Mar. 1988. doi: 10.1086/185121.

C. Greafe, J. Wilms, and U. Heber. Ernst Hartwig: 1851-1923. In G. Wolfschmidt, editor, *Astronomie in Franken*, volume 31 of *Nuncius Hamburgensis – Beiträge zur Geschichte der Naturwissenschaften*, pages 369–387. tredition, Hamburg, 2015. ISBN 78-3-7345-0248-4.

M. Griffiths. Observer's Guide to Variable Stars. Springer Nature Switzerland AG, Cham, Switzerland, 2018. ISBN 978-3-030-00904-5.

Harvard Smithsonian Center for Astrophysics. Chandra Spacecraft, 2008. `https://chandra.harvard.edu/graphics/resources/illustrations/sci_illus_72l.jpg` [Accessed: 2022-03-31].

Harvard-Smithsonian Center for Astrophysics. The Chandra Mission, 2014. `https://chandra.harvard.edu/about/axaf_mission.html` [Accessed: 2022-04-20].

F. Hofmann, W. Pietsch, M. Henze, F. Haberl, R. Sturm, M. Della Valle, D. H. Hartmann, and D. Hatzidimitriou. X-ray source variability study of the M 31 central field using Chandra HRC-I. *Astronomy and Astrophysics*, 555:A65, July 2013. doi: 10.1051/0004-6361/201321165.

K. G. Jones. S Andromedae, 1885: An Analysis of Contemporary Reports and a Reconstruction. *Journal for the History of Astronomy*, 7:27, Jan. 1976. doi: 10.1177/002182867600700103.

P. Kaaret. A Chandra High Resolution Camera Observation of X-Ray Point Sources in M31. *Astrophysical Journal*, 578(1):114–125, Oct. 2002. doi: 10.1086/342475.

P. Kahabka and E. P. J. van den Heuvel. Luminous supersoft x-ray sources. *Annual Review of Astronomy and Astrophysics*, 35(1):69–100, 1997. doi: 10.1146/annurev.astro.35.1.69. URL `https://doi.org/10.1146/annurev.astro.35.1.69`.

C. D. Matzner and C. F. McKee. The expulsion of stellar envelopes in core-collapse supernovae. *The Astrophysical Journal*, 510(1):379–403, jan 1999. doi: 10.1086/306571. URL `https://doi.org/10.1086/306571`.

NASA/CXC/D.Berry. Schematic of Grazing Incidence, X-Ray Mirror, 2009. `https://chandra.harvard.edu/graphics/resources/illustrations/cxcmirrors-72.jpg` [Accessed: 2022-05-30].

V. Ramakrishnan and V. V. Dwarkadas. From Supernova to Remnant: Tracking the Evolution of the Oldest Known X-Ray Supernovae. *Astrophysical Journal*, 901(2):119, Oct. 2020. doi: 10.3847/1538-4357/abb087.

S. P. Reynolds, K. J. Borkowski, D. A. Green, U. Hwang, I. Harrus, and R. Petre. The youngest galactic supernova remnant: G1.9+0.3. *The Astrophysical Journal*, 680(1):L41–L44, may 2008. doi: 10.1086/589570. URL `https://doi.org/10.1086%2F589570`.

M. Sasaki. *Extreme Astrophysics Lecture Notes*. 2020.

M. Sasaki, W. Pietsch, F. Haberl, D. Hatzidimitriou, H. Stiele, B. Williams, A. Kong, and U. Kolb. Supernova remnants and candidates detected in the XMM-Newton M 31 large survey. *Astronomy and Astrophysics*, 544:A144, Aug. 2012. doi: 10.1051/0004-6361/201219025.

F. D. Seward and P. A. Charles. Supernova explosions and their remnants. In *Exploring the X-ray Universe*, page 97–122. Cambridge University Press, 2 edition, 2010. doi: 10.1017/CBO9780511781513.009.

J. K. Truelove and C. F. McKee. Evolution of Nonradiative Supernova Remnants. *Astrophysical Journal, Supplement*, 120(2):299–326, Feb. 1999. doi: 10.1086/313176.

S. van den Bergh. The light curve of s andromedae. *The Astronomical Journal*, 123(4):2045–2046, apr 2002. doi: 10.1086/339314. URL `https://doi.org/10.1086%2F339314`.

A. Acknowledgements

First and foremost, I would like to thank my supervisor Prof. Dr. Manami Sasaki for introducing me to this topic and for the advice and support throughout this work. Thank you to Philipp Weber and Steven Hämmerich for offering their support and to Jonathan Knies for helping me with any Python-related issues. Lastly, I want to thank my family and my friends Nora and Anna for the ongoing emotional support and proof reading.

This work made use of data from the Chandra X-ray Observatory, which is NASA's flagship mission for X-ray astronomy[8]. The data was analysed using the software package CIAO versions 4.12 and 4.14 developed by the Chandra X-ray Center[9] and software provided by NASA's High Energy Astrophysics Science Archive Research Centre (HEASARC)[10].

[8] https://chandra.harvard.edu/
[9] https://cxc.cfa.harvard.edu/ciao/
[10] https://heasarc.gsfc.nasa.gov/docs/software.html

B. Appendix

B.1. Chandra Data Sets

ObsID	Exposure in ks	ObsID	Exposure in ks
9828	19.97	13231	19.49
9829	10.06	13278	18.97
10683	19.90	13279	18.82
10684	18.70	13280	19.29
10838	10.04	13281	18.91
10882	18.85	1912	46.73
10883	18.36	5925	46.29
10884	18.36	5926	28.27
10885	18.27	5927	27.00
10886	18.34	5928	44.86
11808	17.11	6177	20.04
11809	18.42	6202	18.05
12110	19.96	7283	19.94
12111	19.87	7284	20.00
12112	19.94	7285	18.52
12113	18.97	7286	18.71
12114	19.98	8526	19.94
13178	17.45	8527	19.98
13179	17.48	8528	19.98
13180	17.02	8529	18.92
13227	19.99	8530	19.87
13228	19.00	9825	20.21
13229	19.57	9826	19.92
13230	18.93	9827	19.96

Table 6: Observation Identification Numbers (ObsID) of all 45 used Chandra data sets and respective exposure times in ks.

B.2. Python Scripts

B.2.1. Reprocessing Chandra Data Sets

```
from ciao_contrib.runtool import *
import pycrates
import os
import numpy as np


#Generate list of directories
```

```
Path = '/userdata/data/prucker/SAnd/Chandra/'
dirlist = os.listdir(Path)
print(dirlist)

dirlist_cut = []
for k in dirlist:
    if (len(k) == 4 or len(k) == 5):
        dirlist_cut.append(k)

print(len(dirlist_cut))
print(dirlist_cut)

dirlist_updated = dirlist_cut
print(dirlist_updated)

Path_repro = []
for x in dirlist_cut:
    Path_repro.append(Path+x)

print(Path_repro)
print(len(Path_repro))


#run chandra_repro
Repro_2 = Path_repro[2:26]
Repro_3 = Path_repro[26::]
print(Repro_2)
print(Repro_3)

for i in Repro_3:
    chandra_repro.punlearn()
    chandra_repro(indir=i)
```

B.2.2. Calculate Astrometric Corrections

```
from ciao_contrib.runtool import *
import os
import numpy as np

Path = '/userdata/data/prucker/SAnd/Chandra/'
dirlist = os.listdir(Path)

#Generate list of directories/observations
```

```
dirlist_cut = []
for k in dirlist:
    if (len(k) == 4 or len(k) == 5):
        dirlist_cut.append(k)

print(len(dirlist_cut))
print(dirlist_cut)

#remove directories
dirlist_cut.remove('1912')

#remove because wavdetect failed
dirlist_cut.remove('13178')
dirlist_cut.remove('13278')
dirlist_cut.remove('13279')

dirlist_updated = dirlist_cut
print(dirlist_updated)

#-----------------------------------------------------------
#name files
evt2_filename = 'evt2.fits'

#step 2: create psf map
thresh_img_name = 'thresh.img'
psfmap_name = '_all_thresh.psfmap'

#-----------------------------------------------------------

#list of level 2 event files (evt2_files)
Path_repro = []
for x in dirlist_updated:
    Path_repro.append(Path+x+'/repro/')
print(Path_repro)

not_repro_files =np.array([os.listdir(x) for x in Path_repro])
print(len(not_repro_files))
repro_files = np.concatenate(not_repro_files, axis=0)
print(repro_files)

evt2_files = [k for k in repro_files if evt2_filename in k]
print(evt2_files)
print(len(evt2_files))
```

```
#Paths to level 2 event files (evt2_paths)
evt2_paths = [m+n for m,n in zip(Path_repro, evt2_files)]
print(evt2_paths)

#-------------------------------------------------------------

#step 1: run fluximage

#list of paths to directories (obsID) for fluximage
dirpaths_flux=[Path+x+'/fluxed/'+x for x in dirlist_updated]
print(dirpaths_flux)

#actually run fluximage
for i,j in zip(evt2_paths, dirpaths_flux):
    fluximage.punlearn()
    fluximage(infile=i, outroot=j, binsize="8", bands="::1.1")

#-------------------------------------------------------------

#step 2: create psf-map

Path_fluxed = [Path+x+'/fluxed/' for x in dirlist_updated]
print(Path_fluxed)

not_fluxed_files =np.array([os.listdir(x) for x in Path_fluxed
    ])
fluxed_files = np.concatenate(not_fluxed_files, axis=0)

#list of thresh.img
thresh_img_files = [k for k in fluxed_files if thresh_img_name
    in k]

#list of paths to thresh.img
thresh_img_paths = [m+n for m,n in zip(Path_fluxed,
    thresh_img_files)]
print(thresh_img_paths)
print(len(thresh_img_paths))

#list of outfiles for mkpsfmap
outpaths_mkpsfmap = [m+n+psfmap_name for m,n in zip(Path_fluxed
    , dirlist_updated)]
print(outpaths_mkpsfmap)
print(len(outpaths_mkpsfmap))
```

```
#actually run mkpsfmap
for i,j in zip(thresh_img_paths, outpaths_mkpsfmap):
    mkpsfmap.punlearn()
    mkpsfmap(infile=i, outfile=j, energy="1.1", ecf="0.9",
        clobber="yes")
    mode="h"

#-----------------------------------------------------------

#step 3: run wavdetect

#lists of thresh.expmap, thresh.psfmap
expmap_files = [k for k in fluxed_files if 'thresh.expmap' in k
    ]
psfmap_files = [k for k in fluxed_files if 'thresh.psfmap' in k
    ]

#paths to thresh.expmap, thresh.psfmap
expmap_paths = [m+n for m,n in zip(Path_fluxed,expmap_files)]
psfmap_paths = [m+n for m,n in zip(Path_fluxed,psfmap_files)]
print(expmap_paths, len(expmap_paths))
print(psfmap_paths, len(psfmap_paths))


#outfiles for wavdetect (in fluxed directory)
outpaths_wavdetect = [m+n+'_all.src' for m,n in zip(Path_fluxed
    , dirlist_updated)]
outpaths_scell = [m+n+'_all.cell' for m,n in zip(Path_fluxed,
    dirlist_updated)]
outpaths_imagefile = [m+n+'_all.recon' for m,n in zip(
    Path_fluxed, dirlist_updated)]
outpaths_defnbkg = [m+n+'_all.nbkg' for m,n in zip(Path_fluxed,
     dirlist_updated)]

print(outpaths_wavdetect, len(outpaths_wavdetect))
print(outpaths_scell, len(outpaths_scell))
print(outpaths_imagefile, len(outpaths_imagefile))
print(outpaths_defnbkg, len(outpaths_defnbkg))


#actually run wavdetect
for m,n,l,o,p,q,r in zip(thresh_img_paths,psfmap_paths,
```

```
    expmap_paths, outpaths_wavdetect, outpaths_scell,
    outpaths_imagefile, outpaths_defnbkg):
     wavdetect.punlearn()
     wavdetect(infile=m, psffile=n, expfile=l, scales='1 2 4 6 8
         12 16', outfile=o, scell=p, imagefile=q, defnbkg=r,
        clobber='yes')
     mode="h"

#-----------------------------------------------------------

#step 4: run wcs_match

#wcs_match_reffile= '/userdata/data/prucker/SAnd/
    corr_astrometry/10683/repro/10683_all.src' #10683_out.xform
wcs_match_reffile= '/userdata/data/prucker/SAnd/Chandra/1912/
    fluxed/1912_all.src' #1912_out.xform

#list of src_files for wcs_match
src_files = [k for k in fluxed_files if 'all.src' in k]
print(src_files, len(src_files))

#list of paths to src_files
src_paths = [m+n for m,n in zip(Path_fluxed,src_files)]
print(src_paths, len(src_paths))

#list of outfiles for wcs_match
outpaths_wcsmatch = [m+n+'_1912_out.xform' for m,n in zip(
    Path_fluxed, dirlist_updated)]
print(outpaths_wcsmatch, len(outpaths_wcsmatch))

#run wcs_match
for i,j,k in zip(src_paths,outpaths_wcsmatch,thresh_img_paths):
        wcs_match.punlearn()
        wcs_match(infile=i, refsrcfile=wcs_match_reffile,
            outfile=j, wcsfile=k, method="trans", clobber='yes')
```

B.2.3. Apply Astrometric Corrections to Observations

Listing 1: Python Script: Update Astrometric Corrections to Level=2 Event Files

```
from ciao_contrib.runtool import *
import os
import numpy as np
```

```
Path = '/userdata/data/prucker/SAnd/Chandra/'
dirlist = os.listdir(Path)
print(dirlist)

#list of directories/observations
dirlist_cut = []
for k in dirlist:
    if (len(k) == 4 or len(k) == 5):
        dirlist_cut.append(k)

print(len(dirlist_cut))
print(dirlist_cut)

#remove directories
dirlist_cut.remove('1912')

#remove because wavdetect failed
dirlist_cut.remove('13178')
dirlist_cut.remove('13278')
dirlist_cut.remove('13279')

#for 36 observations
#remove because offset wrong
wrong_offset_txt=np.loadtxt('/userdata/data/prucker/SAnd/
   Chandra/txt_files/err_1912_astrometry_corr.txt')
wrong_offset_obsID = [str(int(k)) for k in wrong_offset_txt
   [:,0]]
print(wrong_offset_obsID, len(wrong_offset_obsID))
dirlist_updated = [k for k in dirlist_cut if k not in
   wrong_offset_obsID]

#for all 45 observations
#dirlist_updated = dirlist_cut

print(dirlist_updated, len(dirlist_updated))


#list of level 2 event files (evt2_files)
Path_repro = []
for x in dirlist_updated:
    Path_repro.append(Path+x+'/repro/')
print(Path_repro)

not_repro_files =np.array([os.listdir(x) for x in Path_repro])
```

```
print(len(not_repro_files))
repro_files = np.concatenate(not_repro_files, axis=0)
print(repro_files)

evt2_files = [k for k in repro_files if 'evt2.fits' in k]
print(evt2_files)
print(len(evt2_files))

#Paths to level 2 event files (evt2_paths)
evt2_paths = [m+n for m,n in zip(Path_repro, evt2_files)]
print(evt2_paths)

#Paths to fluxed files
Path_fluxed = [Path+x+'/fluxed/' for x in dirlist_updated]

not_fluxed_files =np.array([os.listdir(x) for x in Path_fluxed
    ])
fluxed_files = np.concatenate(not_fluxed_files, axis=0)

#list of thresh.img
thresh_img_files = [k for k in fluxed_files if 'thresh.img' in
    k]

#list of paths to thresh.img
thresh_img_paths = [m+n for m,n in zip(Path_fluxed,
    thresh_img_files)]
print(thresh_img_paths)
print(len(thresh_img_paths))

#-------------------------------------------------------------

#name files
outfile_asol = '_asol1912_test1_corrected.fits'
out_xform_files = '_1912_out.xform'
evt2_corr_name = '_evt2_1912_test1_corrected.fits'

#-------------------------------------------------------------

#update aspect solution files

#list of asol files
asol_files = [k for k in repro_files if 'asol1.fits' in k]
asol_paths = [m+n for m,n in zip(Path_repro, asol_files)]
print(asol_files, len(asol_files))
```

```
print(asol_paths, len(asol_paths))

#list of corrected asol files
corr_asol_paths = [m+n+outfile_asol for m,n in zip(Path_repro,
    dirlist_updated)]
print(corr_asol_paths, len(corr_asol_paths))

#list of wcs_match outfiles
outpaths_wcsmatch = [m+n+out_xform_files for m,n in zip(
    Path_fluxed, dirlist_updated)]
print(outpaths_wcsmatch, len(outpaths_wcsmatch))

#run wcs_update
for i,j,k,l in zip(asol_paths, corr_asol_paths,
    outpaths_wcsmatch, thresh_img_paths):
     wcs_update.punlearn()
     wcs_update(infile=i, outfile=j, transformfile=k, wcsfile=l,
         clobber='yes')

#-----------------------------------------------------------

#copy evt2 files

#list of copied files
evt2_corrected = [m+n+evt2_corr_name for m,n in zip(Path_repro,
    dirlist_updated)]
print(evt2_corrected, len(evt2_corrected))

#copy files
for i,j in zip(evt2_paths,evt2_corrected):
     dmcopy.punlearn()
     dmcopy(infile=i, outfile=j, option='all')


#-----------------------------------------------------------
#update evt2 files

for i,j,k in zip(evt2_corrected, outpaths_wcsmatch,
    thresh_img_paths):
     wcs_update.punlearn()
     wcs_update(infile=i, transformfile=j, wcsfile=k)


#-----------------------------------------------------------
```

```
#change ASOLFILE keyword values

corr_asol_files = [k for k in repro_files if outfile_asol in k]
print(corr_asol_files, len(corr_asol_files))

for i,j in zip(evt2_corrected,corr_asol_files):
    dmhedit.punlearn()
    dmhedit(infile=i, operation='add', key='ASOLFILE', value=j)
```

B.2.4. Creating Merged Images

```
from ciao_contrib.runtool import *
import os
import numpy as np
import matplotlib.pyplot as plt

Path = '/userdata/data/prucker/SAnd/Chandra/'
dirlist = os.listdir(Path)

#-------------------------------------------------------------
evt2_name = '_evt2_1912_test2_corrected.fits'
evt2_1912 = '/userdata/data/prucker/SAnd/Chandra/1912/repro/
   hrcf01912_repro_evt2.fits'
outroot_name = Path+'merged1912_test3_36obs/'
#-------------------------------------------------------------

#list of directories/observations

dirlist_cut = []
for k in dirlist:
    if (len(k) == 4 or len(k) == 5):
        dirlist_cut.append(k)

print(len(dirlist_cut))
print(dirlist_cut)

#remove directories
dirlist_cut.remove('1912')

#remove because wavdetect failed
dirlist_cut.remove('13178')
dirlist_cut.remove('13278')
```

```
dirlist_cut.remove('13279')

#problem with aspect solution apparently
#dirlist_cut.remove('5925')
#dirlist_cut.remove('6177')
#dirlist_cut.remove('5926')

#for 36 observations
#remove because offset wrong
wrong_offset_txt=np.loadtxt('/userdata/data/prucker/SAnd/
    Chandra/txt_files/err_1912_astrometry_corr.txt')
wrong_offset_obsID = [str(int(k)) for k in wrong_offset_txt
    [:,0]]
print(wrong_offset_obsID, len(wrong_offset_obsID))

dirlist_updated = [k for k in dirlist_cut if k not in
    wrong_offset_obsID]

#for all 45 observations
#dirlist_updated = dirlist_cut

print(dirlist_updated, len(dirlist_updated))

#-------------------------------------------------------------

#list of level 2 event files (evt2_files)
Path_repro = []
for x in dirlist_updated:
    Path_repro.append(Path+x+'/repro/')

not_repro_files =np.array([os.listdir(x) for x in Path_repro])
repro_files = np.concatenate(not_repro_files, axis=0)

evt2_files = [k for k in repro_files if evt2_name in k]

#Paths to level 2 event files (evt2_paths)
evt2_paths = [m+n for m,n in zip(Path_repro, evt2_files)]
evt2_paths.append(evt2_1912)
print(evt2_paths, len(evt2_paths))

#-------------------------------------------------------------

#run merged_obs
```

```
merge_obs.punlearn()
merge_obs(infiles=evt2_paths, outroot=outroot_name, bands
    ='::1.1', binsize='8', clobber='yes')
```

B.2.5. Determine Upper Limit on Source Flux

```
from ciao_contrib.runtool import *
import os
import numpy as np


Path = '/userdata/data/prucker/SAnd/Chandra/'
dirlist = os.listdir(Path)

#list of directories/observations

dirlist_cut = []
for k in dirlist:
    if (len(k) == 4 or len(k) == 5):
        dirlist_cut.append(k)

print(len(dirlist_cut))
print(dirlist_cut)

#remove directories
dirlist_cut.remove('1912')

#remove because wavdetect failed
dirlist_cut.remove('13178')
dirlist_cut.remove('13278')
dirlist_cut.remove('13279')

#for 36 observations
#remove because offset wrong
wrong_offset_txt=np.loadtxt('/userdata/data/prucker/SAnd/
    Chandra/txt_files/err_1912_astrometry_corr.txt')
wrong_offset_obsID = [str(int(k)) for k in wrong_offset_txt
    [:,0]]
print(wrong_offset_obsID, len(wrong_offset_obsID))

dirlist_updated = [k for k in dirlist_cut if k not in
    wrong_offset_obsID]
```

```
#for all 45 observations
#dirlist_updated = dirlist_cut

print(dirlist_updated, len(dirlist_updated))

#-------------------------------------------------------------
#name files
evt2_name = '_evt2_1912_test2_corrected.fits'

out = '/userdata/data/prucker/SAnd/Chandra/
    limit1912_test3_complete/dss3_complete'

evt2_1912 = '/userdata/data/prucker/SAnd/Chandra/1912/repro/
    hrcf01912_repro_evt2.fits'

#SAnd
location = '00:42:43.12368,+41:16:03.2124'
src_file = '/userdata/data/prucker/SAnd/Chandra/SAnd_Area.reg'
bkg_file = '/userdata/data/prucker/SAnd/Chandra/bkg_annulus.reg
    '


#Optical Nova
#location = '00:42:43.11,+41:16:04.2'
#src_file = '/userdata/data/prucker/SAnd/Chandra/Nova_Area.reg'
#bkg_file = '/userdata/data/prucker/SAnd/Chandra/
    nova_bkg_annulus.reg'

#-------------------------------------------------------------

#list of level 2 event files (evt2_files)
Path_repro = []
for x in dirlist_updated:
    Path_repro.append(Path+x+'/repro/')
print(Path_repro)

not_repro_files =np.array([os.listdir(x) for x in Path_repro])
print(len(not_repro_files))
repro_files = np.concatenate(not_repro_files, axis=0)
print(repro_files)

evt2_files = [k for k in repro_files if evt2_name in k]
print(evt2_files, len(evt2_files))

#Paths to level 2 event files (evt2_paths)
```

```
evt2_paths = [m+n for m,n in zip(Path_repro, evt2_files)]

#add 1912 evt2 file
evt2_paths.append(evt2_1912)
print(evt2_paths, len(evt2_paths))

#-------------------------------------------------------------

#run srcflux
srcflux.punlearn()
srcflux(infile=evt2_paths, outroot=out, bands='wide', srcreg=
    src_file, bkgreg=bkg_file, pos=location, psfmethod='quick',
    binsize='8', clobber='yes')
```

B.3. Data X-Ray SNe

Days since discovery	7618	9516	12397	15003	17268
Flux (0.3-8 keV) in 10^{-15} erg cm^{-2}	7.23 ± 1.69	4.59 ± 1.02	2.35 ± 0.60	2.41 ± 1.33	$0.42^{+0.51}_{-0.32}$

Table 7: X-ray fluxes and ages for the light curve of SN1970D in LEDA 31589 (distance $d = 7.2$ MPc) as presented in Ramakrishnan and Dwarkadas (2020). The luminosities L plotted in Figure 19 were calculated from the fluxes and the respective distance d ($L = 4\pi d^2$).

Days since discovery	12466	13406	16153	17744	18000
Flux (0.3-8 keV) in 10^{-15} erg cm^{-2}	4.07 ± 0.90	4.69 ± 0.57	3.02 ± 1.26	2.68 ± 1.24	$0.85^{+1.65}_{-0.84}$

Table 8: X-ray fluxes and ages for the light curve of SN1968D in NGC 6946 (distance $d = 5.5$ MPc) as presented in Ramakrishnan and Dwarkadas (2020). The luminosities L plotted in Figure 19 were calculated from the fluxes and the respective distance d ($L = 4\pi d^2$).

Days since discovery	19550	19775	20811
Flux (0.3-8 keV) in 10^{-15} erg cm^{-2}	10.35 ± 3.19	7.44 ± 1.97	9.12 ± 8.53

Table 9: X-ray fluxes and ages for the light curve of SN1957D in NGC 5236 (distance $d = 4.7$ MPc) as presented in Ramakrishnan and Dwarkadas (2020). The luminosities L plotted in Figure 19 were calculated from the fluxes and the respective distance d ($L = 4\pi d^2$).

Days since discovery	22241
Flux (0.3-8 keV) in 10^{-15} erg cm^{-2}	4.34 ± 1.12

Table 10: X-ray flux and age of SN1941C in NGC 4136 (distance $d = 9.7$ MPc) as presented in Ramakrishnan and Dwarkadas (2020). The luminosity L plotted in Figure 19 was calculated from the flux and the respective distance d ($L = 4\pi d^2$).

C. Eigenständigkeitserklärung

Hiermit bestätige ich, dass die vorliegende Arbeit von mir selbst verfasst wurde, dabei nur die angegebenen Quelllen und Hilfsmittel verwendet wurden und dass sie nicht in wesentlichen Teilen mit einer Arbeit übereinstimmt, die bereits einer anderen Prüfungsbehörde vorgelegt wurde.

Erlangen, 04.07.2022
Ort, Datum

Marie Prucker